Department of Physics and Astronomy
Heidelberg University

Bachelor Thesis in Physics
submitted by

Finn Lubenau

born in Hamburg (Germany)

2022

Dual-comb spectroscopy with free-running frequency combs

This Bachelor Thesis has been carried out by Finn Lubenau at the
Max-Planck-Institute in Heidelberg
under the supervision of
Prof. Thomas Pfeifer
and co-supervision of
Dr. Maximilian Hartmann

Abstract

In the course of this thesis a setup for dual-comb spectroscopy (DCS) was assembled and first experiments performed. The primary aim was to perform proof-of-concept measurements and determine the influence of fluctuations in the repetition rate, as well as in the carrier-envelope frequency of the free-running optical frequency combs. After initial mode-locking of the frequency combs first experiments where performed and the Rubidium D_1 absorption line at 794.760 nm was measured with a spectral resolution of 30 GHz. A numerical simulation of the expected interferograms and respective spectra was performed to compare to the experimental results. Additionally, the effect of small repetition rate fluctuations was investigated in the simulation. Two different averaging methods where performed and compared, stressing the importance of the use of a reference cell with a known spectrum to allow longer time-traces to be averaged. A digital adaptive sampling routine was implemented to the data analysis to allow for longer averaging, significantly improving the resolution.

Zusammenfassung

Im Rahmen dieser Bachelorarbeit wurde ein experimenteller Aufbau für Spektroskopie mittels zweier Frequenzkämme aufgebaut und erste Messungen durchgeführt. Hauptziel dieser Arbeit war es erste Machbarkeitsnachweise zu erbringen, sowie den Einfluss und die Schwere von Fluktuationen in der Repetitionsrate und der Träger-Einhüllenden-Frequenz der nicht referenzierten Frequenzkämme zu bestimmen. Nach erster Modenkopplung konnte die D_1 Absorptionslinie von Rubidium bei 794.760 nm mit einer Auflösung von 30 GHz vermessen werden. Eine numerische Simulation der erwarteten Interferogramme und Spektren wurde durchgeführt, um diese mit den Messergebnissen vergleichen zu können und um die Auswirkungen von Schwankungen in der Repetitionsrate zu bestimmen. Zwei verschiedene Arten zur Mittelung der Ergebnisse wurden durchgeführt und verglichen. Dies zeigte die Wichtigkeit einer Referenzzelle mit bekanntem Spektrum, um längere Mittelungszeiten zu ermöglichen deutlich. Eine digitale adaptive Messkorrektur wurde implementiert und ermöglichte die Mittelung über längere Zeiten, was zu einer Verbesserung der Auflösung führte.

Table of Contents

1. Introduction

Spectroscopy is the domain of science concerned with the study of spectra of electromagnetic radiation as a function of wavelength or frequency. Spectroscopic studies were essential to the development of many subsequent fields in science, laying the foundation for discoveries and vindicating theories.

While the Romans were already aware of the ability to split white sunlight into the colours of a rainbow using a prism, the first theoretical explanations following this experiment were performed by *Isaac Newton* in the 17th century and published in his work "Opticks" in 1704 [20]. In 1802 this setup was improved by *William Hyde Wollaston*, implementing a lens in order to focus sunlight onto a screen, discovering dark lines in the sun's spectrum [29]. By replacing the prism with a diffraction grating, *Fraunhofer* greatly improved the resolution enabling him to quantify the dispersed wavelengths and further analyse the dark lines in the sun's spectrum – today still known as Fraunhofer lines [10]. This reinforces the importance of improved spectral resolution in order to enable new insights in many fields of science. In the early 20th century spectroscopic studies were fundamental to the development of quantum mechanics, providing the basis for the description of the hydrogen atom's spectral lines by *Bohr* and *Schrödinger*.

While for several decades Fourier transform spectroscopy by a Michelson interferometer with a movable mirror was considered the gold standard of spectroscopy, its applications are limited by its principle of operation, since it requires a movable mirror in order to introduce a spatial delay between two light paths [4]. This not only limits its real-time applications, since the mirror must be moved mechanically, but also the minimal size of the system, since the maximum resolution is determined by the available length of the delay stage.

Dual-comb spectroscopy (DCS) overcomes these restrictions by utilising two frequency combs, one of which is slightly detuned with respect to the other, replacing the delay stage by introducing a time delay between two consecutive pulse pairs, thus effectively scanning over each other. As for traditional Fourier transform spectroscopy - as the name suggests - calculating the Fourier transform of the time-trace yields the spectrum. This enables real-time, high resolution, high sensitivity, broadband spec-

troscopy over a wide spectral range without limitations on the instrument's size. In the past, chip sized dual-comb spectrometers have been developed [15], clearly showing the potential of DCS. Additionally, high pulse energies of frequency combs enable measurements over large distances, potentially in the order of kilometres, since the light source and detection device can be arbitrarily separated. Combined with the high resolution possible, DCS could provide real-time measurements of trace gases in the atmosphere in the visible, as well as ultraviolet and infrared spectral region [11].

Current challenges involve stability requirements for DCS-systems, limiting applications to laboratories, where the required stability is attainable, as well as computationally challenging correction algorithms to compensate for fluctuations, limiting its real-time applications [13, 28].

Overcoming these limitations would facilitate many new areas of application, spanning from medical purposes, over pump-probe experiments and trace gas analysis to the analysis of photonic crystals and microscopic quantum dots.

In this thesis, an experimental setup for dual-comb spectroscopy was set up at the *Max-Planck-Institut für Kernphysik* in Heidelberg. The main goal of this work was the generation of heterodyne beating between two frequency combs and calculation of the spectra by performing the Fourier transform of the time-traces (also called interferograms), as well as the determination of the degree of stabilization necessary to allow longer acquisition times. Additionally, computational correction routines were implemented, to correct for fluctuations in the repetition rate difference.

The second chapter of this thesis focuses on the theoretical background behind optical frequency combs and dual-comb spectroscopy. The experimental setup, as well as the results of multiple measurements are presented in the third chapter. In the forth chapter a numerical simulation of the expected time-traces, as well as their respective spectra is presented. Additionally, the influences of repetition rate fluctuations is investigated.

2. Theory

2.1. Frequency combs

Optical frequency combs (OFCs) are a powerful tool that revolutionized the field of spectroscopy because of their broad spectral range and equally spaced frequency modes. The OFCs suitable for spectroscopy are usually generated by stabilization of the pulse train of a mode-locked femtosecond laser, with typical spectra being in the visible to near-infrared (NIR) region. This chapter focuses on the theory behind resonator modes inside the laser cavity 2.1.1, mode-locking those frequency modes 2.1.2, the resulting pulsed laser 2.1.4 and the dispersion and chirp of the femtosecond laser pulses 2.1.3.

2.1.1. Resonator modes

The working principle of a laser is based on an optical oscillator. The laser cavity acts as a resonant optical amplifier whose output is fed back into the system through highly reflective mirrors. Even a small amount of noise with spectral components in the bandwidth of the amplifier's gain curve is sufficient to start the spontaneous emission process. The generated radiation is amplified in a gain medium which typically happens through multiple passes through the medium. Saturation ultimately limits the amplification process, leading to a steady-state output and finite power.
Not all frequencies within the bandwidth of the amplifier are able to oscillate independently. The possible frequencies can be derived by examining the resonator modes inside the laser's cavity, which, for the sake of simplicity, is here assumed to consist of two parallel, fully reflective, flat mirrors that are separated by a distance L.
A monochromatic wave can, only considering the z-dimension, be represented by the complex wavefunction

$$U(z,t) = U(z)\exp(2\pi i\nu t) \tag{2.1}$$

where $U(z)$ denotes the *complex amplitude*, satisfying the Helmholtz equation

$$\nabla^2 U(z) + k^2 U(z) = 0, \tag{2.2}$$

and $k = 2\pi\nu/c$ denoting the wavenumber of a wave with frequency ν inside a medium in which the speed of light is $c = c_0/n$. The possible modes inside the resonator are now given by the solutions of the Helmholtz equation, considering the boundary conditions $U(z = 0) = 0 = U(z = L)$, since the transverse component of the electric field must vanish at the mirror surfaces, i.e. $u(z, t) = \mathrm{Re}\{U(z, t)\}$. A suitable solution considering the boundary conditions is the standing wave $U(z) = A\sin(kz)$, with $kL = q\pi$ and $q \in \mathbb{N}_0$. This restricts the possible frequencies inside the resonator to

$$\nu_q = q\frac{c}{2L} \quad q = 0, 1, 2, ... \tag{2.3}$$

and leads to a spacing between two neighbouring modes of

$$\nu_F = \frac{c}{2L}, \tag{2.4}$$

known as the *Fabry-Pérot intermodal spacing* or *free spectral range* [22].

2.1.2. Mode locking of resonator modes

Since all longitudinal modes derived above are generally able to oscillate independently, they must be coupled by external means in order to generate a frequency comb. This is achieved by mode-locking (also referred to as phase-locking), such that their phases are equal and hence interfere constructively. In the absence of mode-locking all modes for which the gain is greater than the loss begin to grow, and the photons interacting with the medium reduce the gain by lowering the population inversion. Consequently, only the line closest to the central frequency of the gain curve ν_0 (or two lines in the symmetrical case) survives and maintains a gain equal to the loss, reaching steady-state. By mode-locking, all resonator modes that lie within the bandwidth of the active medium interfere, leading to a periodic pulse train in the time- and spatial-domain, as illustrated in figure 2.1 for the spatial domain.

Mathematically one can describe the resonator modes as a comb of Dirac delta functions in the frequency domain, such that

$$\nu_q = \sum_{q=-S}^{S} \delta(\nu_0 + q\nu_F) \tag{2.5}$$

where $M = 2S+1 \approx B/\nu_F$ denotes the (odd) number of modes inside the bandwidth B of the spectrum, ν_0 the central frequency and ν_F the intermodal spacing, as derived in 2.4. This comb in the frequency domain gives rise to pulses in the time domain,

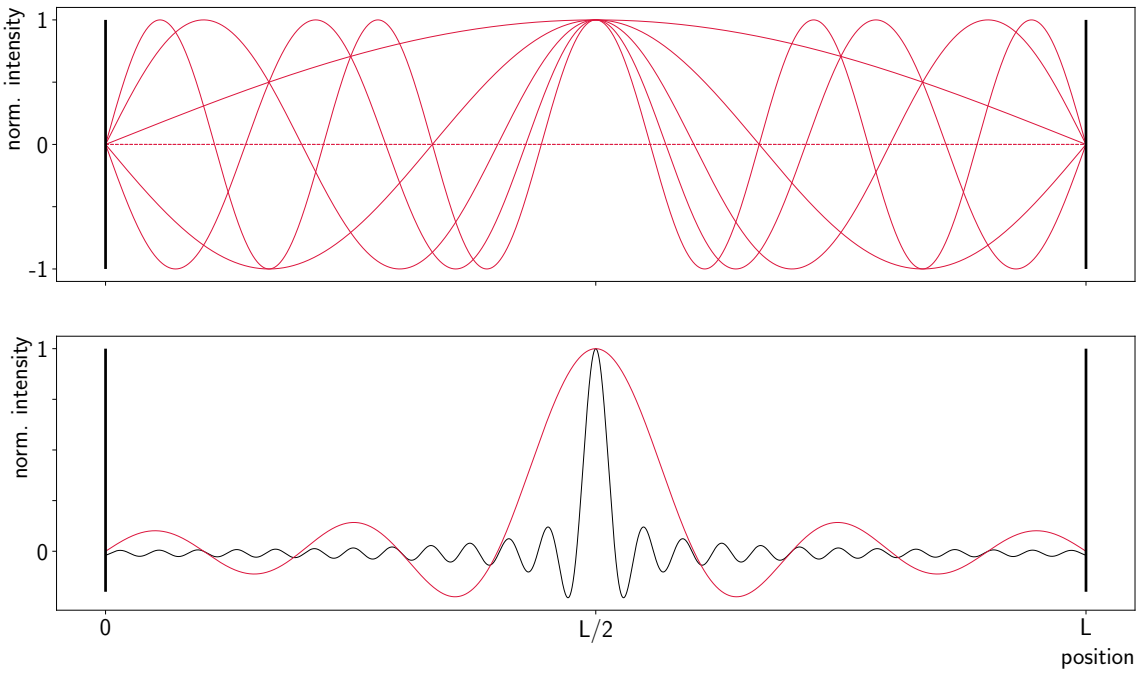

Figure 2.1.: **Illustration of modes inside a resonator cavity. Top:** The first ten standing waves inside the resonator cavity (end mirrors illustrated as vertical black lines). Non-contributing modes are represented by the dashed lines. **Bottom:** Sum of the modes in the top part of the figure (red) and a pulse consisting of the first 31 modes (black). For illustrative purposes the intensity of both pulses has been normalized.

which can be validated by performing the inverse Fourier transform of 2.5:

$$\mathcal{A}(t) = \mathcal{F}^{-1}\left(\sum_{q=-S}^{S} \delta(\nu_0 + q\nu_F)\right) = \int_{-\infty}^{\infty} \sum_{q=-S}^{S} \delta(\nu_0 + q\nu_F)\exp(2\pi i\nu t)d\nu \tag{2.6}$$

$$= \sum_{q=-S}^{S} \exp(2\pi i(\nu_0 + q\nu_F)t) = ... = \frac{\sin(M\pi t\nu_F)}{\sin(\pi t\nu_F)} \tag{2.7}$$

where $\mathcal{F}^{-1}(\cdot)$ denotes the inverse Fourier transform. Since the optical intensity is the absolute square of the complex envelope, i.e. $I(t,z) = |\mathcal{A}(t - z/c)|^2$ the intensity depending on time and position is given by

$$I(t,z) = \frac{\sin^2[M\pi(t - z/c)\nu_F]}{\sin^2[\pi(t - z/c)\nu_F]} \tag{2.8}$$

resulting in pulses with a frequency ν_F, equalling a temporal separation of $t_F = 1/\nu_F$ and a spatial period $2L$.

The pulse duration equals $\tau_{\text{pulse}} = t_F/M \approx 1/\nu_F \cdot \nu_F/\Delta\nu = 1/\Delta\nu$, so, for typical

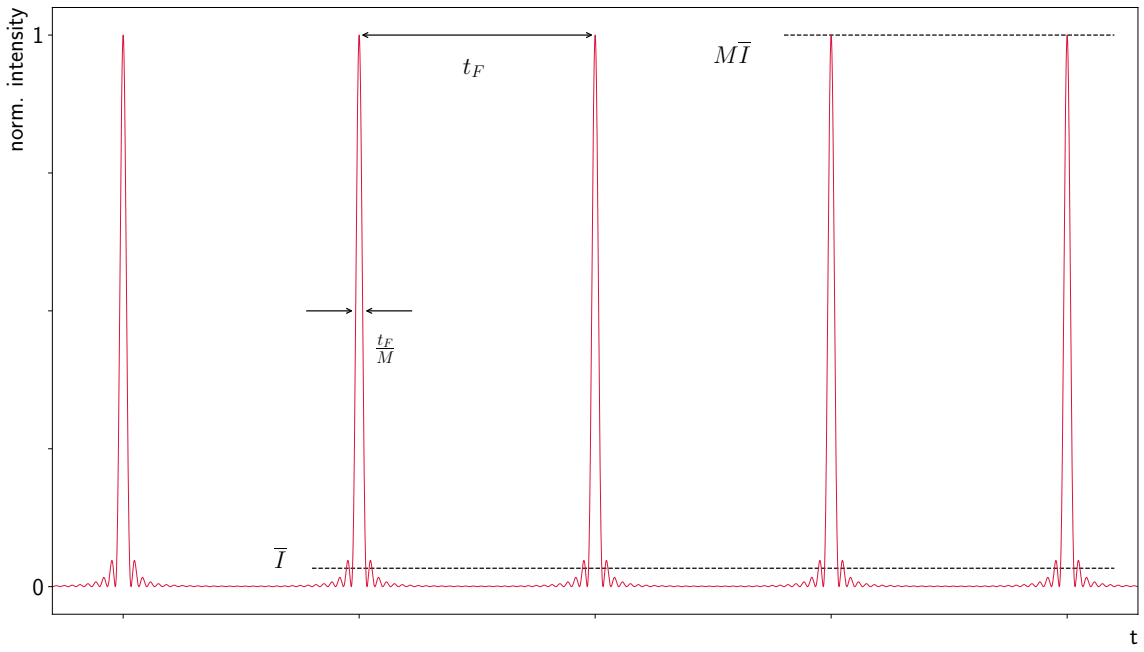

Figure 2.2.: **Pulse train generated by the first $M = 31$ modes.** This corresponds to the spatial picture given in figure 2.1. It can be seen, that the peak intensity $I_{\text{peak}} = M\overline{I}$ is proportional to the number of contributing modes and the pulse width is proportional to the inverse of the number of modes.

spectral widths of $\Delta\nu = 10\,\text{THz}$[1], pulses in the order of femtoseconds ($1\,\text{fs} = 10^{-15}$ s) can be produced. The ratio of the peak intensity to the mean intensity is M, resulting in peak intensities in the order of $\mathcal{O}(100\,\text{kW})$, for a typical mean intensity of 1 W [22].

2.1.3. Dispersion and Chirp of an OFC

In the previous section, the output of an ideal mode-locked laser was examined. This neglected the effect of optical components, i.e. dispersion and broadening of the pulse. In the following, this effect will be discussed, giving rise to the necessity of pulse compression in the OFC.
The *refractive index* of a medium is defined as

$$n = \frac{c_0}{c}, \tag{2.9}$$

where c and c_0 denote the speed of light inside the medium and in vacuum, respectively. Additionally, the refractive index is generally dependent on the wavelength of the transmitted light, i.e. $n = n(\omega)$, where $\omega = 2\pi\nu$ is the *radial frequency*, and thus

$$c(\omega) = \frac{c_0}{n(\omega)}, \tag{2.10}$$

[1]Which corresponds to $\Delta\nu \approx 21\,\text{nm}$.

which is the physical property leading to dispersion, i.e. the frequency dependent speed inside the medium, known as the *phase velocity*. To describe the phenomenon of dispersion on a laser pulse it is useful to first look at the electric field inside the cavity. The electric field of a pulse in the time domain can generally be written as

$$E(t) = \frac{1}{\sqrt{2\pi}} \int_{-\infty}^{\infty} E(\omega) \exp[i\omega t] d\omega, \tag{2.11}$$

where $E(\omega) = \mathcal{F}(E(t))$ denotes the Fourier-transformed electric field.
When a pulse travels through a material, each frequency component gathers a phase $\phi(\omega)$, which leads to an additional phase factor in equation 2.11:

$$e^{i\omega t} \xrightarrow{\text{dispersion}} e^{i\omega t} e^{i\phi(\omega)}. \tag{2.12}$$

To examine the implication of the additional phase factor, it is useful to Taylor expand $\phi(\omega)$ around a central frequency ω_0

$$\phi(\omega) = \phi(\omega_0) + \left.\frac{\partial \phi}{\partial \omega}\right|_{\omega=\omega_0} (\omega - \omega_0) + \frac{1}{2} \left.\frac{\partial^2 \phi}{\partial \omega^2}\right|_{\omega=\omega_0} (\omega - \omega_0)^2 + ... \tag{2.13}$$

$$:= \underbrace{\phi^{(0)}}_{\text{CEP}} + \underbrace{\phi^{(1)} \Delta\omega}_{\text{GD}} + \underbrace{\frac{1}{2} \phi^{(2)} \Delta\omega^2}_{\text{GDD}} + ..., \tag{2.14}$$

where $\Delta\omega = \omega - \omega_0$ denotes the "distance" of a frequency from the central frequency [8]. The effects of these terms differ and are the following:

The **Carrier-envelope phase (CEP)** [rad], also known as *carrier-envelope offset (CEO)*, results from the first term and leads, as the name suggests, to a phase offset between the carrier and envelope frequency, as illustrated in figure 2.3 and represents one of the degrees of freedom of an OFC, as discussed in the following section.

The second term is called **group delay (GD)** [s] and influences the time it takes a pulse to propagate through a medium. The GD is closely connected to the *group velocity* v_{gr} by $v_{\text{gr}} = L/\phi^{(1)}$, where L denotes the length of the dispersive medium. The GD thereby influences the velocity with which the pulse envelope propagates through the medium, but does not change the pulse envelope and consequently does not lead to broadening of the pulse.

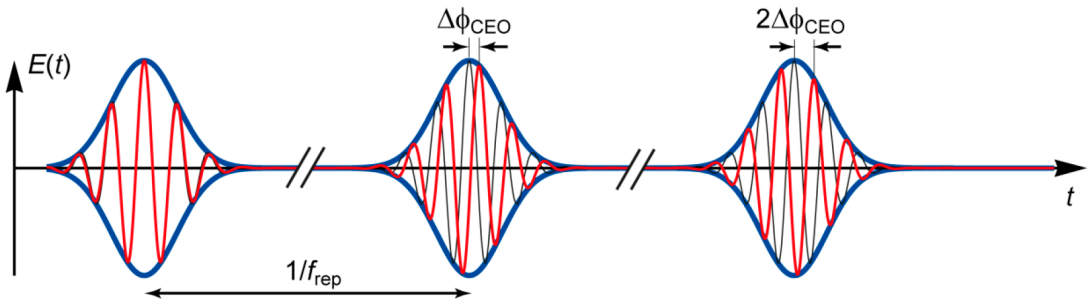

Figure 2.3.: **CEP of pulses in the time domain.** Illustration of the carrier envelope phase Δf_{CEP} resulting from the offset of the carrier phase (red) and its envelope (blue). Image from [25].

The third term is denoted as **group delay dispersion (GDD)** [s^2] and is the lowest-order term responsible for pulse broadening and chirp by dispersion, since the phase difference acquired by propagation is frequency-dependent. This leads to a linear chirp and broadening of the pulse. The GDD can be related to the *group velocity dispersion (GVD)* by GVD = GDD/L, with L denoting the length of the dispersive medium, so the GDD per unit length.

Generally also higher order terms play a role, but are more complicated to account for in experiments. Especially the **third-order dispersion (TOD)** [s^3] may play a role, introducing a quadratic chirp.

2.1.4. Optical frequency combs

There are many different means to generate OFCs, one of them being mode-locked lasers (MLLs). Because MLLs were the original OFC sources and the means used in the scope of this thesis, this section focuses on the description of OFCs using MLLs. As discussed in the previous section, only certain frequencies can oscillate inside the laser cavity, i.e. modes with a frequency spacing of $c/2L$. Additionally, these frequencies are modulated by a common offset frequency arising from the difference in phase- and group-velocity, which leads to an offset in the frequency domain. The frequencies of an OFC can thus be represented by the *comb equation*:

$$\nu_N = f_0 + N f_{\mathrm{rep}}, \quad N = 0, 1, 2, ... \tag{2.15}$$

where f_{rep} denotes the *repetition rate* of the OFC, which is equal to the previously derived resonator mode spacing ($f_{\mathrm{rep}} \equiv \nu_F = \frac{c}{2L}$), $f_0 = \frac{1}{2\pi}\frac{\mathrm{d}}{\mathrm{d}t}\phi_{\mathrm{CEP}}(t)$ denotes the *carrier envelope offset frequency* [9] and N denotes the (non-negative integer) mode

number in the order of $\mathcal{O}(10^6)$, thus allowing the two radio frequencies f_0 and f_{rep} to precisely determine the optical frequency ν_N of a certain mode [4, 6, 21].
To emphasize the difference between radio (rf) and optical (of) frequencies, the symbols f and ν are used for those frequency regimes, respectively.

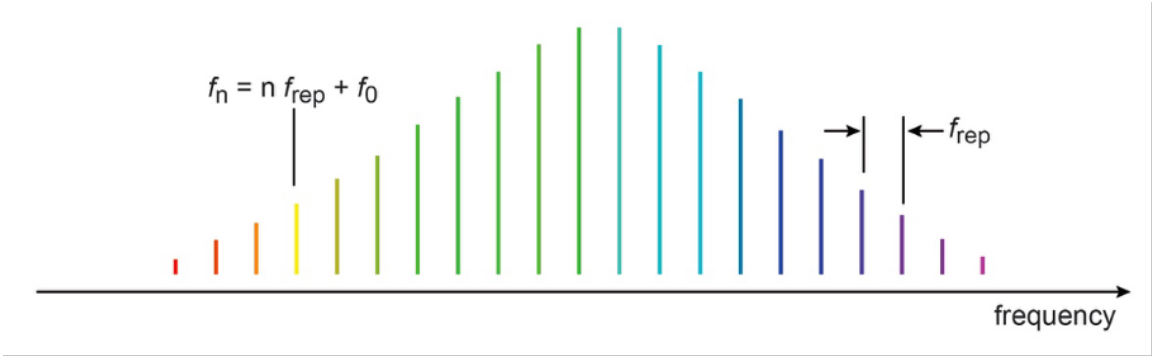

Figure 2.4.: **Illustration of the two degrees of freedom of a frequency comb.** Each comb mode (in this figure denoted as f_n in lieu of ν_N) of a frequency comb is precisely determined by the carrier envelope offset frequency f_0 and the repetition rate f_{rep}. Image from [21].

2.2. Dual-comb spectroscopy

While conventional Fourier transform spectroscopy (FTS), such as in a Michelson interferometer with a movable mirror is considered the gold standard of high-resolution broadband spectroscopy, the mechanical part proves to be the bottleneck of the method (a detailed description of the working principle of FTS with a Michelson interferometer is given in [4]). Firstly, it is responsible for long measurement times, since the delay stage has to be moved mechanically by a significant amount, secondly, it limits the minimum size of the device, since the resolution is fundamentally limited by the optical path-length [6].
To overcome these limitations and outperform traditional FTS, dual-comb spectroscopy (DCS) (in the literature also known as *multiheterodyne spectroscopy, linear optical sampling, coherent Fourier transform spectroscopy* and other designations [6]) replaces the delay stage in a classical interferometer with a second frequency comb. By introducing a small difference in the repetition rates Δf_{rep} of the two frequency combs, a varying time delay $\Delta\tau$ between the two consecutive pulse pairs is achieved, while no moving parts are required. These advantages also allow for nearly instantaneous access to the full bandwidth of the optical spectrum interrogated, limited only by the acquisition speed of the signal processing device.
The use of two OFCs also allows for a large improvement of the spectral resolution and potentially a broad span in any spectral region. However, fluctuations in the repetition rate f_{rep} and carrier-envelope offset f_0 still limit the precision of this technique [13].

2.2.1. Principle

Much like "traditional" FTS, Dual-comb spectroscopy uses the principle of down-converting optical frequencies (which lie in the THz regime) into radio frequencies (MHz regime). This approach enables the resulting radio frequencies (rf) to be measured with conventional photo detectors, which are abundantly available for these frequency regions.
The principle of DCS involves two frequency combs, with slightly different repetition rates f_{rep}, of which at least one probes the sample, thus containing the sample's spectral response. These combs are then spatially overlapped onto a single photo detector, which records the rf signal, the so-called interferogram (IFG).
As described in eq. 2.15 the modes of a frequency comb can be expressed by the simple equation

$$\nu_{N,k} = f_{0,k} + N f_{\mathrm{rep,k}}, \quad N = 0, 1, 2, ... \tag{2.16}$$

with $k = 1, 2$ denoting the first and second OFC, respectively. Since the repetition rates are slightly detuned, they can be written as

$$f_{\mathrm{rep},1} = f_{\mathrm{rep},2} + \Delta f_{\mathrm{rep}}, \tag{2.17}$$

with $\Delta f_{\mathrm{rep}} \ll f_{\mathrm{rep},1}, f_{\mathrm{rep},2}$. The arbitrary assumption $f_{\mathrm{rep},1} > f_{\mathrm{rep},2}$ was made. The spatial overlap of the wavefronts on the photo detector creates a beating signal consisting of the sum and difference frequencies of the signal, in analogy to a frequency mixer [12, 13, 24, 28].
The difference frequencies are in the order of $\mathcal{O}(\Delta f_{\mathrm{rep}}) = 100\,\mathrm{Hz}$ and can be detected with the photo detector, whereas the sum frequencies are in the order of $\mathcal{O}(\nu_n) = 100\,\mathrm{THz}$, and therefore suppressed by the low-pass characteristic of the photo detector [12]. This low-pass characteristic should not be confused with the actual low-pass[2] used in the experiment, as photo detectors are simply unable to time resolve frequencies in the THz region since their bandwidth is not sufficient (if this was the case DCS would become void, since spectroscopic measurements could be performed with a single OFC). The difference frequencies between individual modes of the two OFCs can be expressed by

$$\begin{aligned} \nu_{n+l,1} - \nu_{n,2} &= [f_{0,1} + (n+l) f_{\mathrm{rep},1}] - [f_{0,2} + n f_{\mathrm{rep},2}] \\ &= [f_{0,1} - f_{0,2}] + n[f_{\mathrm{rep},1} - f_{\mathrm{rep},2}] + l f_{\mathrm{rep},1} \\ &\coloneqq \Delta f_0 + n \Delta f_{\mathrm{rep}} + l f_{\mathrm{rep},1} \end{aligned} \tag{2.18}$$

where $\nu_{n+l,1}$ and $\nu_{n,2}$ denote the (n+l)-th and n-th mode of OFC one and two, respectively. From this equation it becomes clear, that the beating frequency of "next-neighbouring" modes, i.e. modes of n-th and $(n+1)$-th order, is modulated by the frequency $\Delta f_{\mathrm{rep}} + \Delta f_0 + f_{\mathrm{rep},1}$. Beating between all orders of modes with all other orders of modes occurs, but since higher order beat modes do not contain additional information, a low-pass filter is used to exclude those frequencies from the data acquisition and the resulting interferogram. If only the beat signal of neighbouring modes is considered eq. 2.18 simplifies to

$$\nu_{N,1} - \nu_{N,2} = \Delta f_0 + N \Delta f_{\mathrm{rep}}, \quad N = 0, 1, 2, ... \tag{2.19}$$

[2] A low-pass filter is used to suppress the beating frequencies of non-neighbouring modes. See section 3.3.1 for details.

which is the governing equation of DCS, since it gives rise to the down-conversion of optical frequencies into the radio frequency regime, if the difference in repetition rates is chosen accordingly, typically Δf_{rep} is in the order of $\mathcal{O}(100\,\mathrm{Hz} - 1\,\mathrm{kHz})$. This down-conversion can be quantified by the *down-conversion coefficient* a, which can be deduced by comparing eq. 2.16 and 2.19 and is given by

$$a = \frac{\Delta f_{\mathrm{rep}}}{f_{\mathrm{rep}}}, \tag{2.20}$$

where the reasonable approximation $f_{\mathrm{rep}} = f_{\mathrm{rep},1} \approx f_{\mathrm{rep},2}$ was made [6, 12, 13, 24, 28]. The down-conversion and mode spacing is illustrated in figure 2.5. Typical down-conversion coefficients are in the order of $\mathcal{O}(a) = 10^{-5}$.

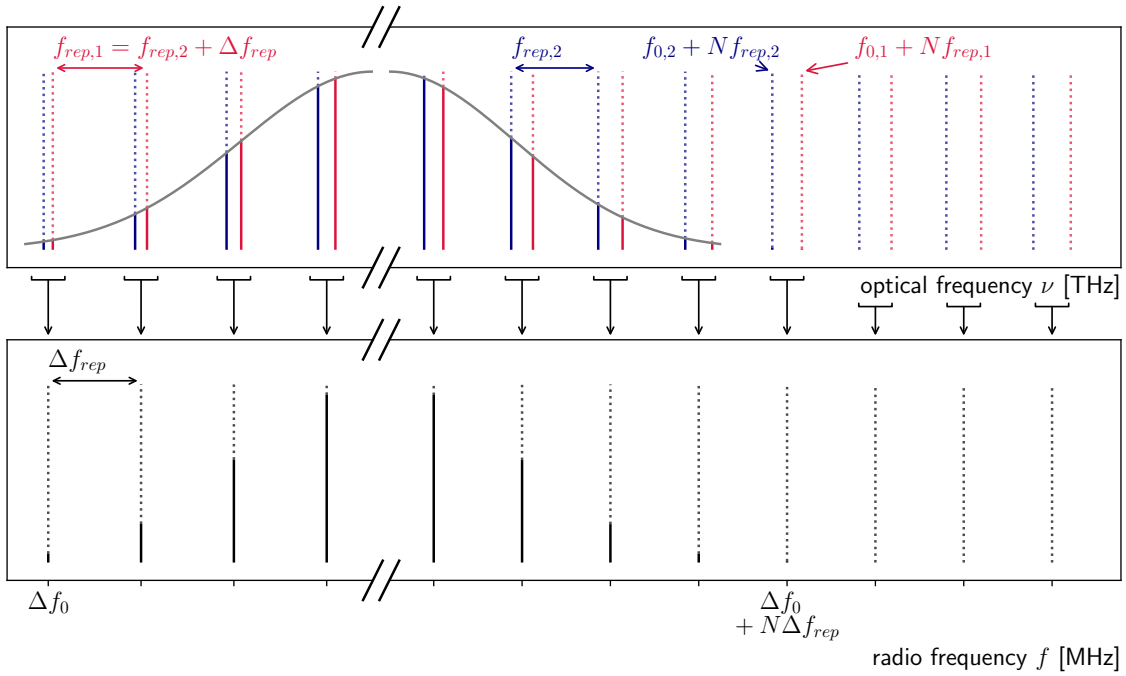

Figure 2.5.: **Down-conversion of optical frequencies to radio frequencies. Top**: Two OFCs (red and blue) with slightly detuned repetition rates are overlapped and generate beating frequencies in the rf-regime. The grey curve represents the spectra of the OFCs. **Bottom**: Resulting heterodyne difference frequencies in the radio frequency regime.

In the time-domain the difference in repetition rates equals a linear time delay $\Delta\tau$ between consecutive pulse pairs, analogous to the delay stage used in traditional FTS. This time delay is given by

$$\Delta\tau = \frac{1}{f_{\mathrm{rep}}} - \frac{1}{f_{\mathrm{rep}} + \Delta f_{\mathrm{rep}}} = \frac{\Delta f_{\mathrm{rep}}}{f_{\mathrm{rep}}(f_{\mathrm{rep}} + \Delta f_{\mathrm{rep}})} \approx \frac{\Delta f_{\mathrm{rep}}}{f_{\mathrm{rep}}^2} \tag{2.21}$$

and is in the order of 10 fs to 100 fs.

2.2.2. Down-conversion, resolution and acquisition time

To achieve the resolution required for a given problem the difference in repetition rate Δf_{rep} between the two lasers must not be chosen arbitrarily, but in accordance with the Nyquist–Shannon sampling theorem which relates the required sampling rate, denoted f_s, to the desired bandwidth that one wishes to acquire. This optimum repetition rate difference also avoids aliasing of the beat modes, such that only the beating of neighbouring modes contributes to the interferogram and an unambiguous assignment is possible. This leads to the condition $\Delta f \leq f_{\mathrm{rep}}/2$, where Δf denotes the bandwidth of the down-converted (rf) spectrum (see figure 2.6). This bandwidth relates to the optical bandwidth via $\Delta f = a\Delta\nu$ resulting in

$$\Delta f = a\Delta\nu \leq \frac{f_{\mathrm{rep}}}{2} \Leftrightarrow a \leq \frac{f_{\mathrm{rep}}}{2\Delta\nu}. \tag{2.22}$$

This restriction of the down-conversion factor therefore determines the maximum repetition rate difference via eq. 2.20 as

$$\Delta f_{\mathrm{rep}} \leq \frac{f_{\mathrm{rep}}^2}{2\Delta\nu}. \tag{2.23}$$

As long as the difference in repetition rate is fulfilling this condition the beat modes of the same order do not overlap with beat modes of different orders (cf. eq. 2.18). To ensure that only frequencies of interest are measured, a low-pass filter is used to suppress the beating of non-neighbouring modes, suppressing frequencies greater than $f_{\mathrm{rep}}/2$.

The resolution of DCS is, unlike that of traditional FTS, not determined by the maximum path difference that can be achieved, but by various other parameters. One of the limiting factors is the stabilization of f_{rep} and f_{CEO}, since fluctuations cause broadening in the optical resonator modes and therefore broadening in the beat modes. These effects can be mitigated either by stabilizing or measuring these frequencies, such that fluctuations can be suppressed or accounted for in retrospect [4, 12, 13]. For more details of computational methods to correct for those fluctuations one can refer to other works e.g. [13, 28].
If the conditions for the repetition rate difference in 2.23 are met, and thus the beating frequencies do not exceed $f_{\mathrm{rep}}/2$, the Nyquist–Shannon sampling theorem states that in order to fully capture the information in the interferogram, the sampling rate f_s must be greater or equal than the higher repetition rate, so $f_s \geq f_{\mathrm{rep},1}$ [4, 6, 12, 13, 15, 17, 21].

To determine the resolution of the down-converted frequency domain, a measurement length of t_{M} is considered. In this time the number of samples taken is $t_{\mathrm{M}} f_s$,

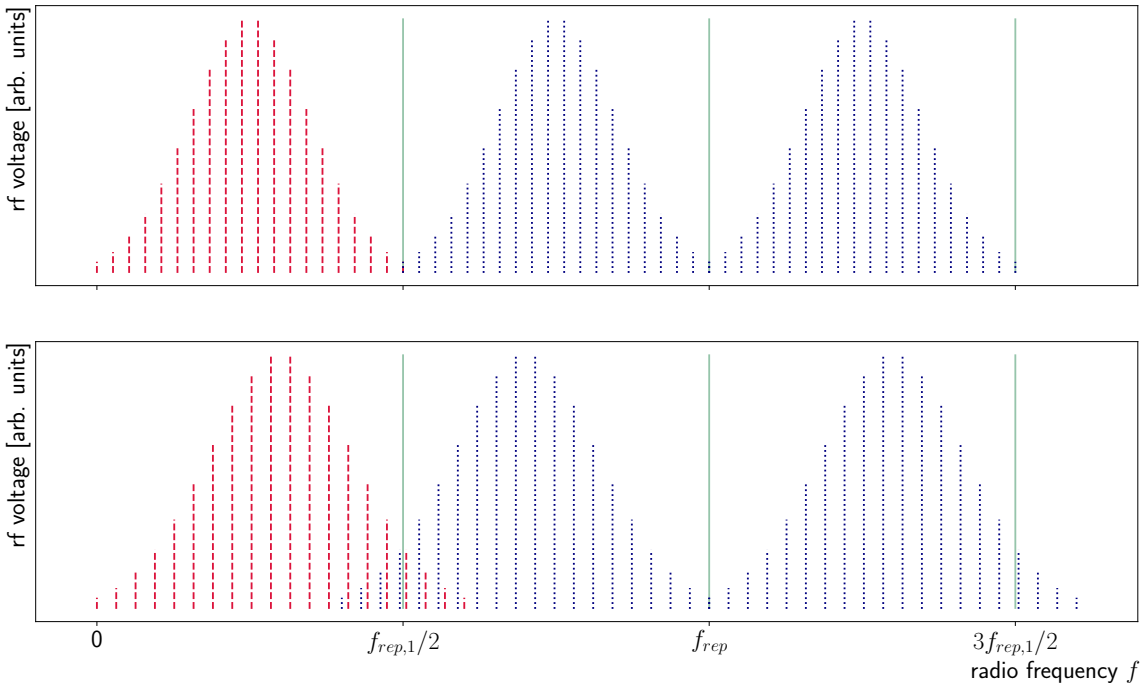

Figure 2.6.: **Illustration of clean and corrupted beat modes. Top:** Beat modes in the rf-regime in the optimal case of $\Delta f = f_{\mathrm{rep}}/2$, so an unambiguous assignment is possible. **Bottom:** Beat modes in the case of $\Delta f > f_{\mathrm{rep}}/2$. Beat modes of next-neighbouring modes start to overlap with beat modes of neighbouring modes, the assignment becomes ambiguous.

which leads to a resolution of

$$\delta f(t_{\mathrm{M}}) = \frac{\Delta f}{t_{\mathrm{M}} f_s}, \tag{2.24}$$

and in the ideal case of $f_s = f_{\mathrm{rep}}$ and $\Delta f = f_{\mathrm{rep}}/2$ to

$$\delta f(t_{\mathrm{M}}) = (2t_{\mathrm{M}})^{-1}. \tag{2.25}$$

It should be noted that the resolution can only be improved by increasing the measurement time, not by increasing the sampling rate, since the full spectral information can be recovered by any sampling frequency $f_s \geq 2\Delta f$. Fundamentally, the resolution is only limited by the combs' linewidth, since spectral features that lie too close to each other can not be resolved [6]. Hence, the resolution in the optical domain is given by

$$\delta\nu(t_{\mathrm{M}}) = (2t_{\mathrm{M}}a)^{-1} \geq \frac{\Delta\nu}{t_{\mathrm{M}} f_{\mathrm{rep}}} \tag{2.26}$$

and the maximum resolution is achieved, when $a = f_{\mathrm{rep}}/2\Delta\nu$ (cf. eq. 2.22) [4, 12].

2.3. Rb-Atom

Rubidium (Rb) with its two natural isotopes ^{85}Rb (stable) and ^{87}Rb (radioactive) has two characteristic transitions in the red part of the visible spectrum at 794.760 nm (D_1) and 780.241 nm (D_2) justifying its name[3]. In this thesis, the D_1 transition between the $5^2S_{1/2}$ and $5^2P_{1/2}$ states of ^{85}Rb is measured. The natural linewidth of this transition is $\Gamma = 2\pi \cdot 5.7500(56)$ MHz [27] with a Doppler-broadened FWHM of $\Delta f_{\mathrm{FWHM}} = 402.23$ MHz at 160 °C. The transition lines and their respective hyperfine splitting are shown in figure 2.7 for the D_1 transition.

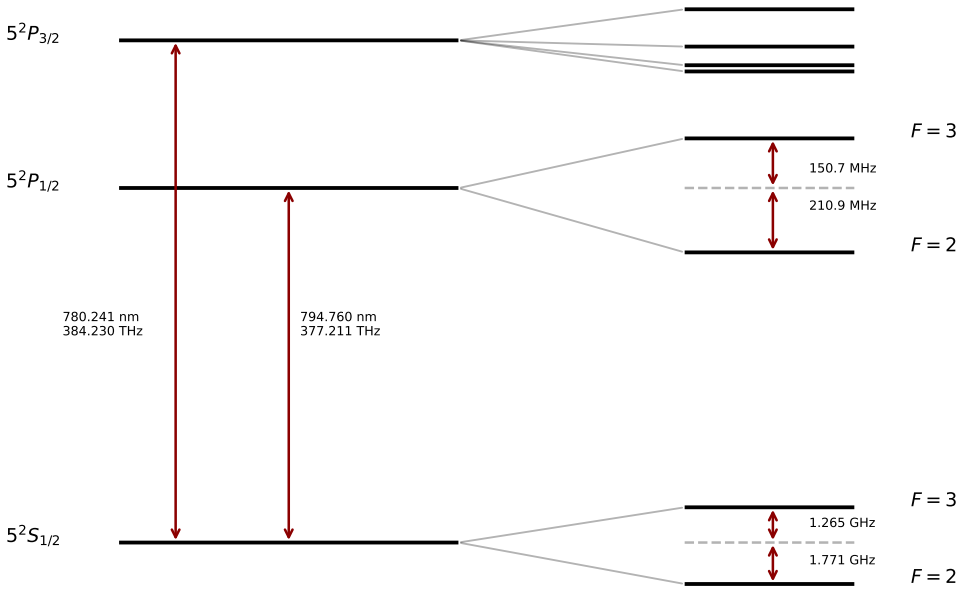

Figure 2.7.: **Rubidium $^{85}_{37}$Rb D_1 and D_2 hyperfine structure.** The hyperfine splitting is shown for the D_1 transition (794.760 nm, 377.211 THz) and suggested for the D_2 transition (780.241 nm, 384.230 THz), however since the D_2 transition was not measured in the course of this thesis, no relative hyperfine shifts are plotted. The hyperfine shifts and D_2 transition frequency are taken from [27], the D_1 transition frequency from [1].

[3] From the Latin *rubidus*, meaning *deep red*.

3. Experimental Setup and Results

The setup used in this thesis mainly consists of two mostly identical optical frequency combs (OFCs) (see section 2.1) and an optical (beam) path in order to generate the heterodyne and the resulting rf spectrum by overlapping the two pulses as described in section 2.2.
Section 3.1.1 focuses on the pump lasers and the required changes to the OFCs, due to malfunction of one of the pump lasers. An overview of the OFCs is given in section 3.1.2 and section 3.1.3 and 3.1.4 focuses on the AOM[1] used for mode-locking and the prism sequence for dispersion compensation, respectively.

The experiment is located in the experimental halls (*Experimentierhalle*) at the *Max-Planck-Institut für Kernphysik* in Heidelberg, Germany in a laser laboratory, including air conditioning and dust protection, to ensure as little disturbance by environmental influences as possible.

3.1. Pump laser and Oscillator

The laser system used in this experiment is a commercially available mode-locked titanium-sapphire (Ti:Al_2O_3, abbreviated as Ti:Sa) laser by *Spectra-Physics*, i.e. a *Tsunami Model 3960*. The lasers are capable of operating in the femtosecond (fs) as well as picosecond (ps) regime, in this experiment solely used in their fs configuration. Since one of the laser systems (OFC1) was initially in its ps configuration, the system had to be converted to its fs configuration, which required installing a prism sequence, changing the positions of mirrors M_4 and M_5 (see fig. 3.1) and removing the installed birefringent filter. Additionally, a highly reflective mirror (M_1) (see fig. 3.3) had to be installed, which is not used in the ps configuration[2]. Further changes due to insufficient pump power of this systems' pump laser are described in 3.1.1.
The OFCs consist of a Ti:Sa rod pumped by a *Millennia* pump laser in a folded cavity with 12 mirrors, four prisms, a tunable slit for wavelength adjustments, the required electronics for mode-locking and other optical elements.

[1] Acousto-optic modulator
[2] In the ps configuration a GTI (Gires-Tournois Interferometer) is installed at the position of the HR. It compensates the negative GVD, instead of the prism sequence used in the fs configuration.

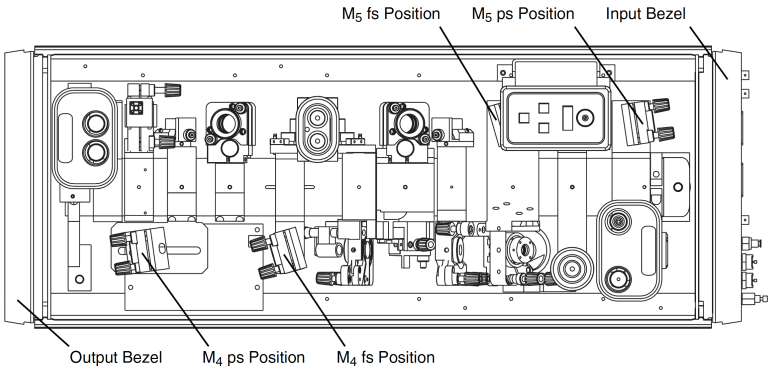

Figure 3.1.: **Positions of mirrors M_4 and M_5 in ps and fs configuration.** Image taken from *Spectra-Physics* manual.

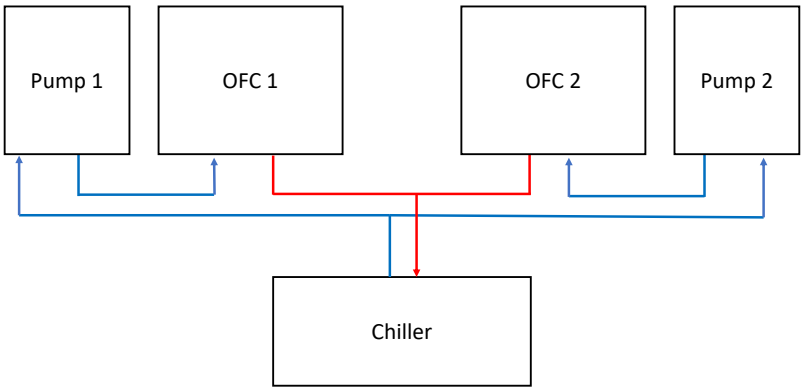

Figure 3.2.: **Coolant lines interconnect diagram.** The outlet of the chiller (blue) is split into two separate coolant lines, leading first into the pump laser and afterwards into the OFC, for both lasers respectively. The back flow (red) goes back into the chiller.

To ensure temperature stabilization, the OFCs and pump lasers are water cooled by a chiller, with water at a temperature of 18 °C as specified in the manual. A schematic overview over the coolant line connections is shown in figure 3.2. To prevent heating of the laboratory and unnecessary noise disturbance, the chiller is placed outside the laboratory and the water inlet as well as the outlet are fed through the laboratory wall. To ensure sufficient flow to the laser systems, the maximum diameter of coolant lines was chosen, i.e. 10 mm for the direct flow out of the chiller split into two 6 mm lines leading to each of the laser systems, as specified by the manufacturer.

3.1.1. Pump lasers

The two pump lasers used to pump the Ti:Sa rod are diode-pumped, continuous wave (cw) solid state laser of the same type, however they differ in their maximum

output power P_{pump}. The pump laser for OFC1 is a model *Millennia XV* capable of 15 W cw output power, while the pump laser for OFC2 is a *Millennia X* with a maximum power of 10 W. The first pump laser did not achieve its full power and was reduced to a 10 W system, which required installing a different output coupler (OC) in OFC1. The available replacement optics were limited in wavelength range and subsequently the broadband high-reflector of OFC1 was moved to OFC2, therefore OFC1 is operated with a limited bandwidth, spanning from 780 nm to 900 nm.
Since, in the course of this thesis, the pump laser for the first laser system started to malfunction and is unable to maintain the intended output power of 8.4 W, the system was reduced to 7.4 W. The other pump laser does not have this issue and is set to an output power of 8.2 W. The output power of each pump laser is adjustable via separate controllers, along with other settings, e.g. the position of the shutter or the diode currents.
The lasers are four level, neodymium yttrium vanadate (Nd:YVO_4) scheme, which, in turn, is pumped by a $\lambda_0 = 808$ nm semiconductor laser diode, populating the $^4F_{5/2}$ level, with an energy of 1.53 eV relative to the ground state, which decays rapidly to the $^4F_{3/2}$ level. From this level, lasing is achieved by the $^4F_{3/2} \rightarrow {}^4I_{11/2}$ transition at 1064 nm [22, 23]. The 1064 nm line is frequency doubled by lithium-triborate crystal (LBO), generating the required 532 nm line (second harmonic) for pumping the Ti:Sa rod. A detailed description is given in Appendix A.

3.1.2. Oscillator overview

An overview of the cavity and the electronic controls of the OFCs is given in figure 3.3. Two mirrors (P_1 and P_2) are used to couple the pump laser beam into the Ti:Sa rod and subsequently guided through the Ti:Sa rod by mirrors M_2 and M_3. The approximate cavity length is 1.874 m, designed as a folded cavity, allowing for a compact oscillator system. Mirror M_1 is a highly reflecting mirror, that can be electronically driven via the *Tsunami Model 3930* for coarse changes of the cavity length. Fine adjustments of the cavity length can be performed with mirror M_4, controlled by a piezo-electric motor, allowing for rapid adjustments and stabilization of the repetition rate. The repetition rate is monitored by a photodiode, which receives a small amount of light by a beam splitter behind the cavity. However, due to malfunctions of the electronic controls of the *Tsunami Model 3930* for the second laser system, no stabilization was possible for the respective OFC.

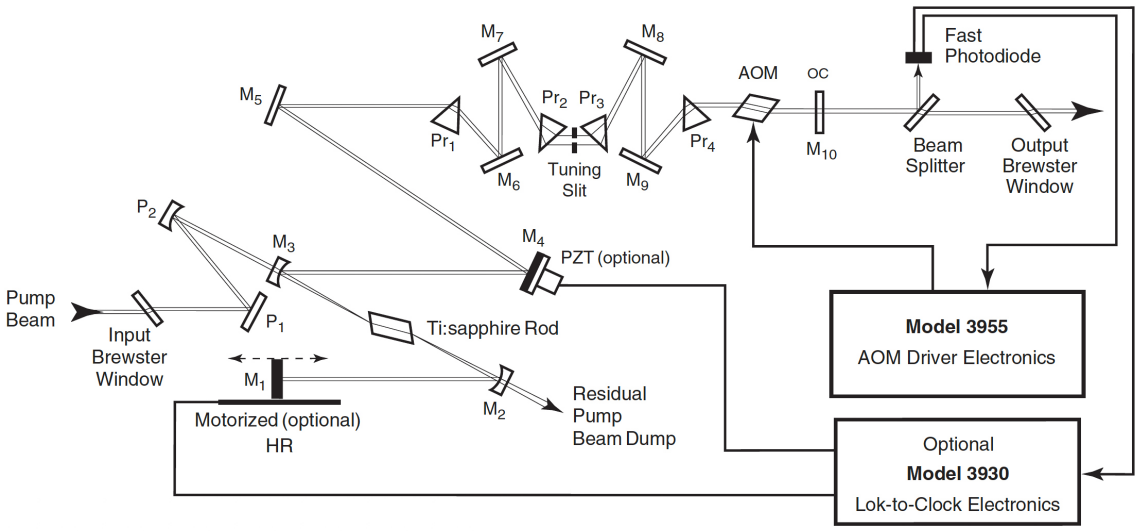

Figure 3.3.: **fs configuration of the OFCs.** Overview over the beam path inside the cavity. M, Pr, HR, PZT and AOM denote mirrors, prisms, the high-reflector, the piezo-controlled mirror and the acousto-optic modulator, respectively. The connection to the control electronics is shown schematically by arrows. Image taken from *Spectra-Physics* manual.

3.1.3. Mode-locking with an acousto-optical modulator

As described in section 2.1.2 all frequency modes generally oscillate independently and have random phases resulting in continuous output out of the laser. To achieve mode-locking an acousto-optic modulator (AOM) is placed just before the cavity end mirror and controlled by the *Tsunami Model 3955* electronics, introducing a time dependent loss inside the system. Only when the phases of the longitudinal modes happen to be equal, these pulses are able to pass the AOM undiffracted and without loss, which leads to mode-locking. Once mode-locking is achieved, the oscillator continues to be mode-locked even if the AOM is disabled since the phases of the longitudinal modes continue to be equal. On the front panel of *Tsunami Model 3955*, the phase between the photodiode signal and the AOM can be adjusted by a range of 100 ps to ensure proper mode-locking.

3.1.4. Prism compressor for dispersion compensation

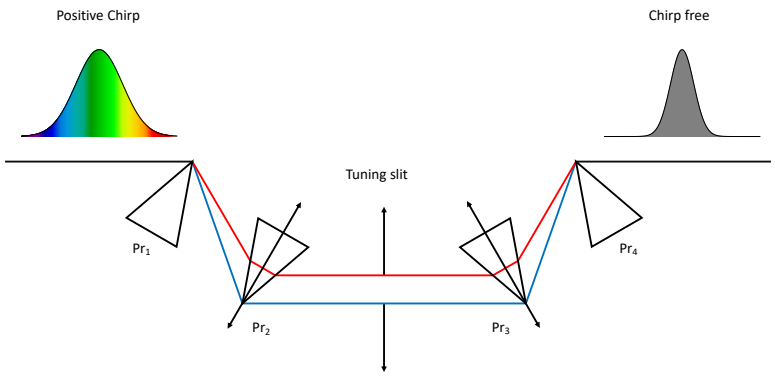

Figure 3.4.: **Prism compressor used for dispersion compensation.** The incoming pulse (black line) has a positive Chirp, i.e. the red frequencies are at the leading edge of the pulse. In the prism compressor the pulse experiences a negative GVD since red frequencies (red line) have a longer path through the prisms than higher frequencies (blue line), hence compensating for the positive GVD, which leads to a shorter pulse.

To account for the group velocity dispersion (GVD) and self-phase modulation (SPM) by an intensity-dependent refractive index $n(I)$

$$n = n_0 + n_2 I, \tag{3.1}$$

of a nonlinear medium (the Ti:Sa rod) due to the *optical Kerr effect* (n_0 and n_2 denote the linear- and non-linear refractive index [2, 22], respectively), the oscillator contains a prism compressor for dispersion compensation.
The prism compressor consists of four prisms, denoted Pr_1 through Pr_4, four mirrors (M_6 to M_9) to guide the beam through the prisms and a variable slit (see fig. 3.4). The slit, as well as prisms Pr_2 and Pr_3 can each be adjusted by a micrometer head on top of each OFC, to select a wavelength range and account for its specific dispersion. The slit width determines the wavelength range and can be adjusted by a screw on top of the OFC. It is not intuitively obvious that the prism compressor allows the higher frequencies to "catch up" with the lower frequencies, since the difference in pathlengths seems to be inverted. However, the sign of the GVD depends on the second derivative of the path length P with respect to the wavelength λ, resulting in a negative GVD as a result of the angular dispersion as shown by Martinez et al. [19] which compensates the positive GVD values of the other optics. Consequently, the prism compressor results in a chirp-free, Fourier transform limited output pulse [3].

3.2. Pulse characterisation

In this chapter, important properties of the OFCs are determined and discussed. This includes the determination of the emitted spectra, the pulse structure and the output power of the OFCs. These quantities are essential for a proper execution of the experiment, as discussed in the following.

3.2.1. Power measurements

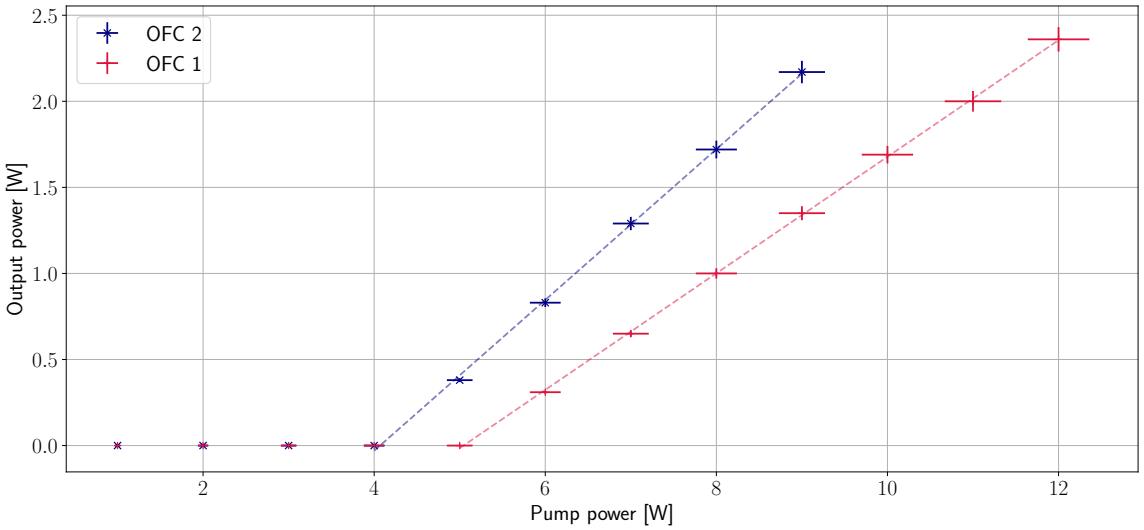

Figure 3.5.: **Determination of the lasing threshold.** The output power of the OFCs was measured against the pump power for each OFC. As the pump power exceeds the lasing threshold the output power increases linearly with the pump power.

In order to determine the lasing threshold of the OFCs, the output power was measured as a function of the pump power, for both OFCs respectively. This is depicted in figure 3.5 and shows the expected linear dependence of the output power on the pump power, as soon as the pump power exceeds the lasing threshold. The lasing threshold was determined to be $P_{\text{threshold}} = 5.044(3)\,\text{W}$ for OFC1 and $P_{\text{threshold}} = 4.068(7)\,\text{W}$ for OFC2, respectively. The pump power used in the subsequent experiments equals $P_{\text{pump},1} = 7.4\,\text{W}$ and $P_{\text{pump},2} = 8.2\,\text{W}$ for OFC1 and 2, respectively, as discussed in section 3.1.1.

The output power greatly depends on the position of the cavity end mirrors, as well as the prism and slit configuration. The OFCs are configured to emit roughly $P_{\text{OFC1}} = 1\,\text{W}$ and $P_{\text{OFC2}} = 1.5\,\text{W}$.

3.2.2. Spectral measurements

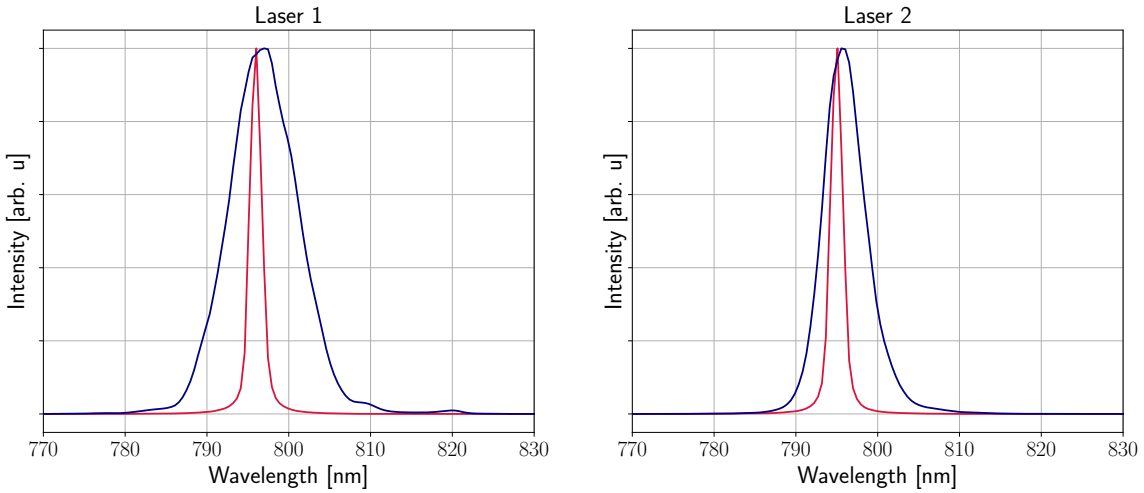

Figure 3.6.: **Spectra of the OFCs.** Comparison between the non mode-locked spectra (red) and the mode-locked spectra (blue). Mode-locking significantly broadens the spectra from a cw line (FWHM of 1.5 nm due to the spectrometer resolution) to a spectral width greater than 25 nm.

One important property of the OFCs are their spectra. Firstly, it is important that the spectra overlap to generate the heterodyne beating between the resonator modes of the OFCs. Secondly, the spectral width determines the maximum difference in repetition rate allowed for an unambiguous assignment of the comb modes (cf. eq. 2.6) and thereby fully covering the spectral width available.
The spectra are recorded with two *Ocean Insight STS-NIR* CMOS spectrometers, capable of a resolution of 1.5 nm and an available wavelength range of 650 nm – 1100 nm. Light is coupled into the spectrometer by a beam splitter placed directly behind the cavity of the OFC, reflecting a small amount of light into an optical fibre, leading to the spectrometer for each OFC, respectively.
It should be noted that one of the two available spectrometers is not wavelength-calibrated and therefore not suitable for precise measurements, although qualitative measurements are possible since the spectral width and features can be measured nonetheless.
The spectra of the OFCs are tunable between 780 nm to 900 nm, limited by the mirror reflectivity, and are mostly operated around 800 nm for the subsequent measurements. The spectral width and shape depends on the alignment of the prism compressor, as well as the width of the slit (c.f. fig. 3.4). Typical spectra are shown in figure 3.6. In the absence of mode-locking the spectra consist of a single cw line, with a width of 1.5 nm (FWHM) due to the resolution of the spectrometer. Once mode-locking is established, the spectra broaden significantly to up to 10 nm FWHM and

30 nm FWTM (full width at tenth maximum). During the course of the experiment, the spectra were changed frequently to optimize the covered spectral range for the intended measurement and to ensure proper mode-locking.

3.2.3. Photo-diode measurements

The time-traces of the OFCs' pulses (see figure 3.7) indicate, whether or not single pulses are emitted. Single pulses show the typical response of the photo-diode (PD), with a steep leading edge and an exponential "decay" of the signal after the pulse. By adjusting the prism and slit sequence conditions for double pulses can be met, resulting either in a time-trace with a steep leading edge and an approximately linear decay if the pulses are faster than the PD fall time, or double-periodic pulses. Changing the position of the prisms and slit allows to suppress double pulses if occurring. However, this also changes the spectral width and shape, so these adjustments must be tuned and iterated.
The PD used is a *ThorLabs DET025A/M* linear silicon-based photo-diode, capable of detecting the required bandwidth and a rise and fall time of 150 ps, respectively. This does not allow recording the femtosecond pulses of the OFCs in detail, but to determine their repetition rate and to record the interferograms.
The time-traces of the PD are recorded with a *Rhode & Schwarz* model *RTM3004* oscilloscope, capable of recording 5 GSa/s (Gigasample per second). With a sampling frequency of 80 MHz time-traces with a length of 80 MSa can be recorded, corresponding to a maximum measurement time of 1 s, although the length is halved when two channels are used.
The OFCs' repetition rate was measured to be around 80 MHz (corresponding to a temporal separation between pulses of approximately 12.5 ns). However, a precise measurement of the repetition rate is unfeasible without further data analysis, since the internal counter of the oscilloscope only provides the frequency with a resolution of $\mathcal{O}(100\,\mathrm{Hz})$.
A typical measurement of the repetition rate and the PD response can be seen in figure 3.7, clearly showing the phenomenon of double pulses. Between the large peaks resulting from the "main" pulse, smaller peaks can be seen. If pulses in the cavity split into multiple pulses and have a temporal separation greater than the pulse width, this leads to measurable double (or potentially multiple) pulses in the cavity. Since the time separation of the double pulses in figure 3.7 equals half the cavity round trip time (12.5 ns), this corresponds to two pulses, one at each end of the cavity. This highlights the importance of proper mode-locking and the mitigation of double-pulses.

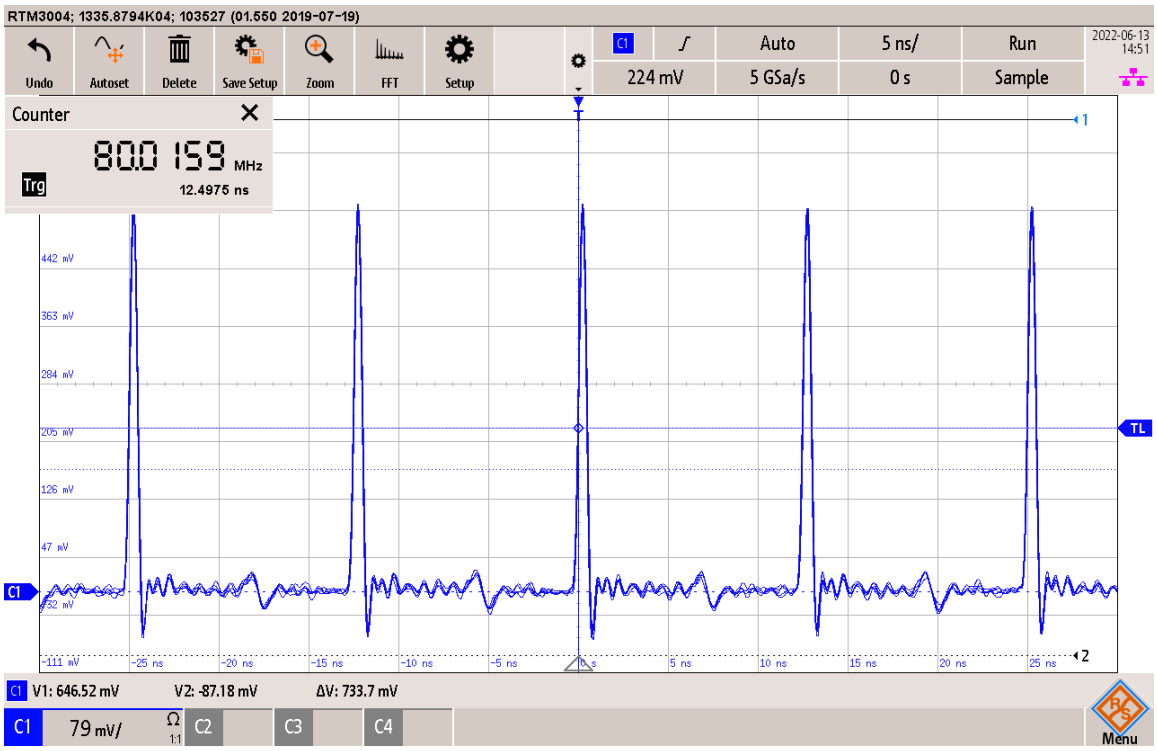

Figure 3.7.: **PD response of pulses on the oscilloscope.** The steep leading edge and the exponential decay of the PD response can be seen. During this measurement the repetition rate was measured to be 80.0159 MHz and small double-pulses can be seen between the larger peaks.

3.3. Measurements of Rubidium-Spectra

3.3.1. Setup

In order to test the experimental setup and subsequent data analysis, the spectrum of Rubidium (Rb) is measured. This serves as a proof-of-concept experiment for the setup and determines whether the lack of stabilization of the repetition rate f_{rep} for the first OFC (cf. eq. 2.3) and the lack of stabilization of the carrier-envelope offset frequency f_{CEO} prevents to record time-traces and generate spectra by performing the Fourier transform.
In order to generate heterodyne beating between the two OFCs, the beam of each of the combs is focused onto the photo-diode and a 50:50 beam splitter is used to overlap both beams. To generate a sufficient heterodyne beating, the beams must precisely overlap both in the horizontal and vertical direction. To ensure overlap in the vertical direction, the height of one of the beams directly behind the cavity of the OFC is taken as a reference height, which is maintained for both beams at any distance behind the cavity and the subsequent mirrors. This ensures a coarse overlap on the photo-diode. Fine adjustments for a continuous overlap behind the beam splitter are made by two mirrors in front of the beam splitter, for each OFC respectively.

To record the Rb absorption spectrum, one of the beams interacts with the sample, i.e. it passes through a cell filled with Rb twice, adding to a total interaction length of 40 mm. The cell is heated to 160 °C by means of a homemade temperature control unit and a voltage supply with a power of approximately 15 W leading to an estimated atomic density of $2.8 \times 10^{14}\,\mathrm{cm}^{-3}$ inside the cell [18]. Both beams are then overlapped onto the photo-diode. The signal of the photo-diode is recorded with the oscilloscope and stored by a laboratory computer for the subsequent data analysis of the time-trace. A schematic overview of the setup is given in figure 3.8. To ensure sufficient spatial beating between the laser beams focused on the PD, an iris aperture is used to prevent diffracted parts of the beam to be measured by the PD. Additionally, to suppress the comb repetition rate $f_{\mathrm{rep}} \approx 80\,\mathrm{MHz}$ and higher-order beating signals with frequencies $f > 40\,\mathrm{MHz}$, a low-pass filter (LP) is connected to the PD signal output. The LP has a bandwidth of 36 MHz, ensuring that frequencies $f > 40\,\mathrm{MHz}$ are fully suppressed, and the interferogram can be recorded without any ambiguity from beat modes that contain no additional information.
The repetition rate of both OFCs can be measured with the photodiode output of the *Tsunami Model 3955* for both of the laser systems, respectively and is displayed on the front panel with an accuracy of 100 Hz. Since the generated spectrum only

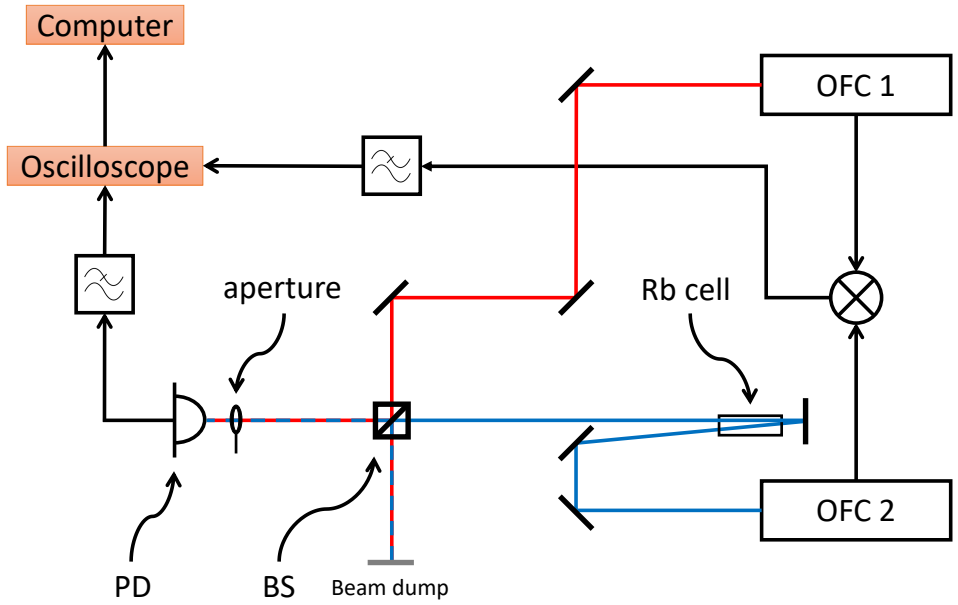

Figure 3.8.: **Schematic overview of the setup for the measurement of Rb-Spectra.** One laser beam passes through the Rb-cell and overlaps with the other beam behind the beam-splitter (BS) and is measured with a photo-diode (PD) and recorded with an oscilloscope connected to a computer. The repetition rate of each laser is used to determine the difference frequency with a frequency mixer.

depends on the difference in repetition rates Δf_{rep} (c.f. eq. 2.19), a frequency mixer is used to generate the heterodyne, i.e. the sum and difference frequencies of both signals:

$$f_{\mathrm{rep},1} + f_{\mathrm{rep},2} = [f_{\mathrm{rep},2} + \Delta f_{\mathrm{rep}}] + f_{\mathrm{rep},2} \approx 2 f_{\mathrm{rep},2} \qquad \text{and} \tag{3.2}$$

$$f_{\mathrm{rep},1} - f_{\mathrm{rep},2} = [f_{\mathrm{rep},2} + \Delta f_{\mathrm{rep}}] - f_{\mathrm{rep},2} = \Delta f_{\mathrm{rep}}, \tag{3.3}$$

where the reasonable assumption $\Delta f_{\mathrm{rep}} \ll f_{\mathrm{rep},2}$ was made in the former equation. By applying a low-pass filter, the sum frequency is suppressed and only the difference frequency is measured with the internal trigger counter of the oscilloscope. This allows the repetition rate difference Δf_{rep} to be adjusted in real time, thereby fully exploiting the frequency range available in the rf-domain, as described in section 2.2.2. Recording the repetition rate difference allows for a comparison of the measured difference and the spacing of the bursts of the interferogram, which have a repetition period of $1/\Delta f_{\mathrm{rep}}$. This provides a sanity check for the subsequent data analysis. Generally, those two methods resulted in coinciding values.

3.3.2. Results

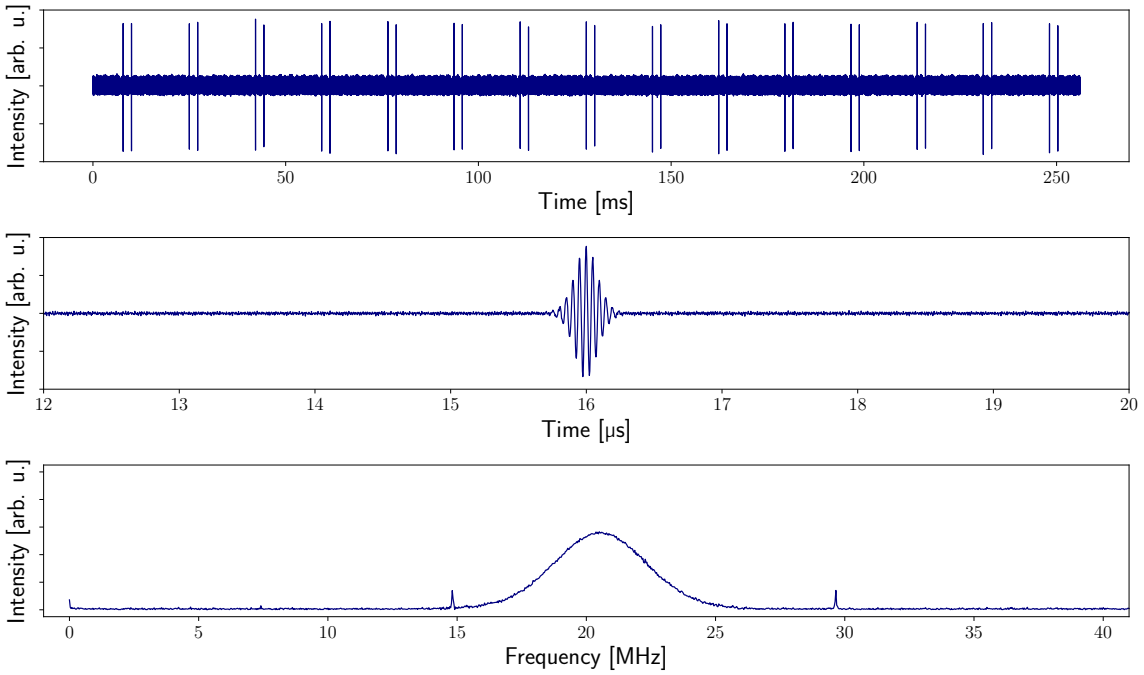

Figure 3.9.: **First recorded interferogram. Top:** 256 ms long time-trace showing double bursts which result from double-pulses from one of the OFCs (see text for details). **Middle:** Averaged IFG burst calculated from all bursts after phase correction **Bottom:** Fourier transform of the averaged IFG burst in the rf regime.

In the following section, the experimental results of the performed measurements are presented and analysed. The first meaningful measurements were recorded after the setup and configuration of the oscilloscope was completed and data could be recorded in an efficient manner.

The first interferograms (figure 3.9, top) were recorded in order to provide a proof-of-concept measurement and to determine the degree of data analysis and correction necessary to retrieve spectra from the interferograms (IFGs). At this point only one channel was recorded and no data from the frequency mixer is available.
A 256 ms time-trace was recorded with a sampling frequency of $f_s = 313\,\mathrm{MHz}$. Although this sampling frequency is higher than the required 80 MHz for a lossless reconstruction of the spectrum, a high sampling frequency enables a detailed analysis of the single bursts of the IFG. Since bursts in the IFG arise from the overlap of pulses from the OFCs, these burst have a time separation of $\Delta t_{\mathrm{bursts}} = 1/\Delta f_{\mathrm{rep}}$. Taking a closer look at the IFG shows that the bursts are not equally spaced, but show a double-periodic behaviour. The second bursts are shifted by $\Delta t_{\mathrm{IFG}} = 2.16\,\mathrm{ms}$ in the IFG. This is likely caused by double pulses of one of the OFCs. To determine

the shift of the second pulse, with respect to the first pulse Δt_{pulse}, one needs to look at the time delay between two consecutive pulse pairs, as calculated in equation 2.21:

$$\Delta\tau = \frac{\Delta f_{\text{rep}}}{f_{\text{rep}}^2}. \tag{3.4}$$

This time delay multiplied by the number of pulses that are between the first and second burst, i.e. $\Delta t_{\text{IFG}}/(1/f_{\text{rep}})$, yields the time shift of the double pulses:

$$\Delta t_{\text{pulse}} = \frac{\Delta t_{\text{IFG}}}{1/f_{\text{rep}}} \frac{\Delta f_{\text{rep}}}{f_{\text{rep}}^2} \tag{3.5}$$

$$= \Delta t_{\text{IFG}} \frac{\Delta f_{\text{rep}}}{f_{\text{rep}}}. \tag{3.6}$$

Analysing the distance of the double bursts yields a repetition rate difference of $\Delta f_{\text{rep}} = 58.0\,\text{Hz}$. With the above equation and a repetition rate of $f_{\text{rep}} = 80.0\,\text{MHz}$ this leads to a second pulse shifted by $\Delta t_{\text{pulse}} = 1.57\,\text{ns}$, with respect to the first one. Since the carrier envelope phase (CEP) differs for every burst in the IFG, a phase shift has to be introduced in order to allow averaging. For this, the Hilbert transform of the real-valued time-trace is performed and the phase is determined. This phase is then corrected for each burst, such that the CEP is zero, and the bursts are subsequently averaged. This provides the $32\,\mu\text{s}$ long averaged interferogram, of which a cutout is depicted in the middle part of figure 3.9. An example of the performed phase correction is shown in figure B.1.

Fourier-transforming this averaged IFG burst results in the Gaussian spectrum of the heterodyne beating of the OFCs depicted in the bottom part of figure 3.9. The FWHM of the spectrum equals 4.26 MHz in the rf interferogram, which corresponds to an optical spectral width of 5.88 THz. This does not fully exploit the optimal spectral range of 40 MHz since the frequency analysis via heterodyne beating was not yet implemented and Δf_{rep} could not be adjusted in real time. This highlights the importance to determine the repetition rate difference in real time since the data analysis is computationally challenging, due to the large amount of data points and adjusting Δf_{rep} with the analysed IFG is not feasible in practice. The rf spectrum has a total width of 11 MHz, so, following from equation 2.23, the ideal repetition rate difference for this spectral width is $\approx 210\,\text{Hz}$, leading to a spectrum approximately 3.6 times broader, which fully covers the unambiguous range.

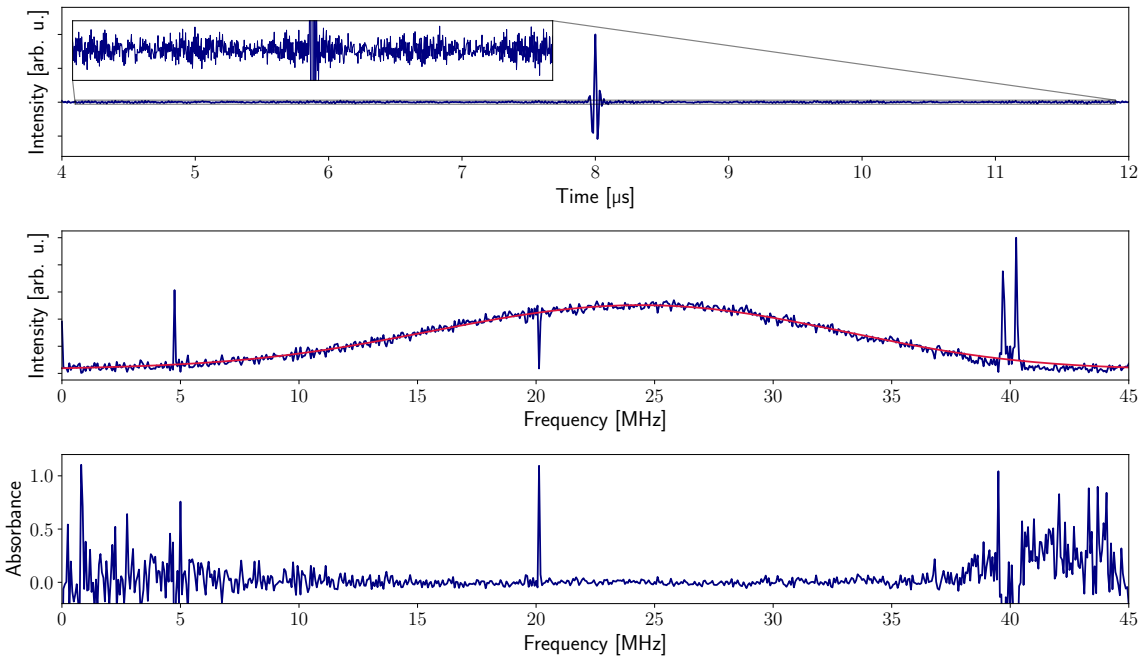

Figure 3.10.: **First interferogram with the Rb sample. Top:** Average burst calculated by averaging over all bursts in the IFG, after phase correction. **Middle:** Spectrum after Fourier-transformation of the average burst (blue) and low-pass filtered spectrum for absorbance calculation (red). **Bottom:** Absorbance of the Rb sample.

Subsequently, the same setup configuration was used to measure the Rb sample. Reducing the sampling frequency to $f_s = 80\,\mathrm{MHz}$, allows for a 640 ms long time-trace to be recorded. This time-domain IFG is shown in figure B.2 in the appendix. Again, the double periodic burst structure is visible, caused by double pulses separated by 0.147 ns. As for the previous measurement, the spectrum was calculated by averaging the corrected interferometric bursts and performing the Fourier transform. This was done for the full, as well as one-tenth of the time-trace, as shown in figure B.3 and 3.10, respectively, the upper parts of both figures show the averaged burst, the middle parts depict the spectrum after Fourier-transformation (blue) and the low-passed spectrum (red), used to calculate the absorbance, depicted in the lower parts. It is clearly visible, that averaging more bursts leads to "washing-out" of the spectral features, due to fluctuations of the repetition rate, as well as carrier envelope offset of the OFCs. Analysing the 64 ms part of the IFG clearly shows the Rb D_1 absorption line at 794.760 nm with a resolution of 30 GHz (0.063 nm).

In order to improve the resolution and diminish the influence of repetition rate fluctuations, the difference in repetition rate is measured with a frequency mixer, as described in section 3.3.1. With the knowledge of Δf_{rep} at any time during the

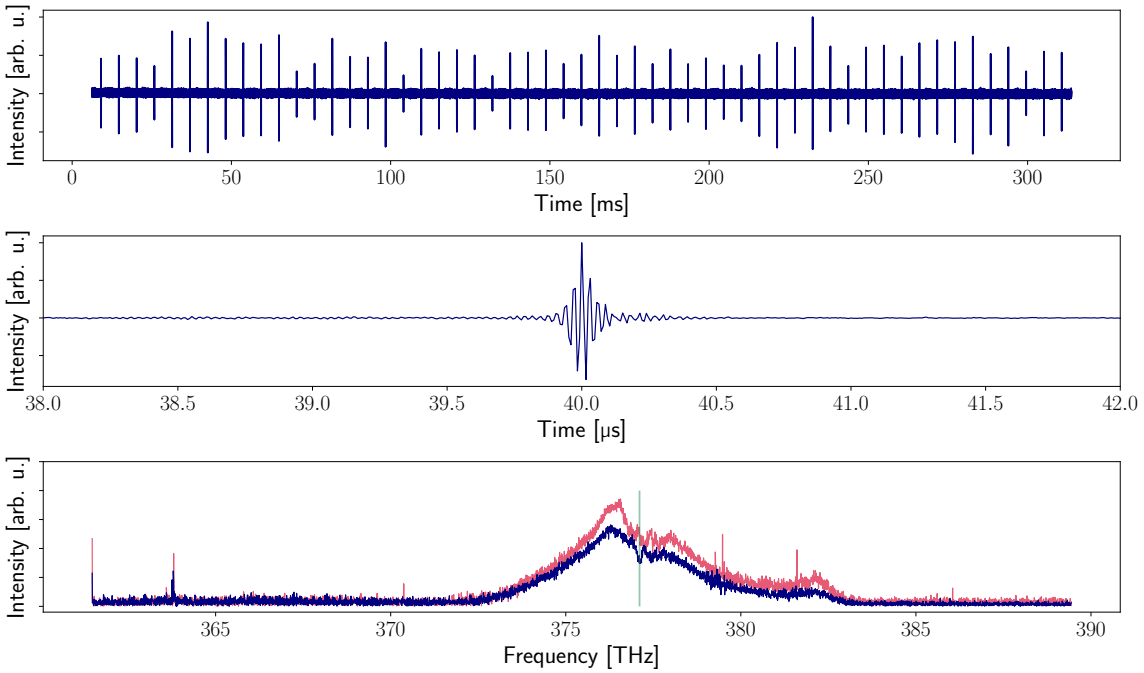

Figure 3.11.: **Time-domain IFG measured with the Rb cell. Top:** Time-domain IFG of the measurement with Rb. **Middle:** Averaged IFG burst with the adaptive sampling routine. **Bottom:** Fourier-transformation of the averaged IFG burst for the with (blue) and without (red) adaptive sampling. The green line indicates the Rb transition line at 794.760 nm. The dip in the adapted spectrum is clearly visible, while the non-adapted spectrum shows multiple dips at different positions.

measurement, an adaptive sampling method is implemented. In principle this is similar to methods described elsewhere, e.g. [30], hence only the differences are discussed here. One key difference between those methods is, that in lieu of adjusting the sampling frequency during the measurement the implemented method records the signal of the frequency mixer and the recorded IFGs are subsequently corrected. This ensures that the data points are not equally spaced, but adjusted such that the recorded IFGs are not disturbed by fluctuations of the repetition rates of the OFCs. The low-pass filtered Δf_{rep} signal is recorded, Hilbert-transformed and the angle, i.e. the phase and the corresponding frequency is determined by means of a python data analysis routine. Since small fluctuations in the recorded time-trace greatly influence the determined instantaneous frequency, a smoothing routine is used to reduce the noise of the signal. Introducing this adaptive sampling routine greatly increases the resolution of the measurements. Figure 3.11 shows the recorded data with the Rb cell in the optical path (c.f. setup scheme in figure 3.8).

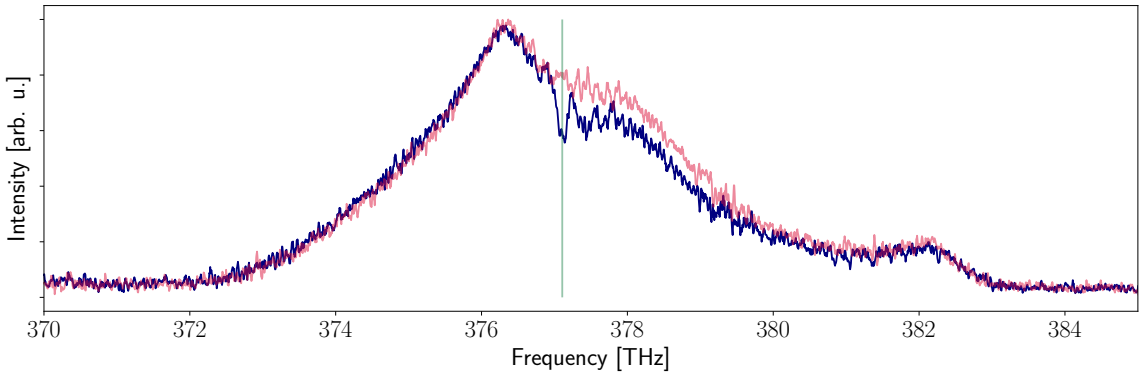

Figure 3.12.: **Comparison of the spectrum with (blue) and without (red) the Rb cell in the optical path.** This figure clearly shows the Rb absorption line (green), despite a slightly different spectral shape.

The 314 ms long time-trace is shown at the top of figure 3.11 and is recorded with a sampling frequency of 125 MHz, in order to provide a sufficient resolution while maximizing the available length of the time-trace, since the recording length is halved when recording two channels simultaneously. In contrast to the data recorded previously, this data does not show the double-periodic structure, indicating that the OFCs are sufficiently mode-locked and tuned to suppress double-pulses. The repetition rate difference was measured to be 179 Hz with a deviation of 0.1 Hz between the determination with the frequency mixer and the distance of the peaks, respectively. As before, the single bursts of the IFG are averaged into a single 80 μs long IFG, shown in the middle plot of 3.11, that reveals the modulation due to the polarization decay [7]. Fourier-transforming the averaged IFG leads to the spectrum shown at the bottom of figure 3.11. From this spectrum it is clearly visible that the adaptive sampling (blue) greatly improves the visibility of the Rb transition line, whose position is indicated by the green vertical line, in contrast to the non-adapted data (red). Since an absolute frequency reconstruction is possible if the repetition rate difference and the absolute position of a spectral feature are known, this data could be up-converted from the rf to the of-domain, using the Rb D_1 transition line at 794.760 nm (377.211 GHz) [1] to calculate the offset. The width of the optical spectrum is 10.4 THz (22 nm) spanning from 782.8 nm to 804.6 nm, thus the maximum repetition rate difference that allows unambiguous assignment of the beat modes is $\Delta f_{\mathrm{rep,max}} = 307.7$ Hz, above the measured repetition rate difference of 179 Hz. The Rb D_1 absorption line at 794.760 nm could be resolved with a resolution of 240 GHz (0.51 nm).

To verify that the visible dip in the spectrum of the Rb measurement is not a spectral artefact, but the Rb absorption, figure 3.12 shows the comparison of the recorded Rb spectrum and a spectrum recorded under the same conditions, i.e. with the same

sampling rate, repetition rate difference and spectral width of the OFCs, but with the Rb cell at a low temperature, thus effectively only the Rb gas "removed" from the optical path without removing the sample cell. The spectrum without Rb was up-converted using the position of the maximum of the spectrum, since no distinct spectral feature is available without any absorption line. Comparing these spectra clearly shows the Rb absorption at 377.211 THz, although the spectral shape changed slightly in between those two measurements. Since the spectra are slightly different, calculating the absorbance did not yield meaningful results. The IFG for the measurement without Rb is shown in figure B.4 in the appendix.

Since the measurement with Rb contains an absolute spectral feature, it is possible to average over the spectra of the single bursts of the IFG, rather than averaging over the bursts. Performing the Fourier transform of a 80 μs long time window around the centre of the bursts yields the rf spectra depicted in the upper part of figure 3.14. Here the fluctuation of Δf_0 is clearly visible by the differing offset from zero. Up-conversion of the rf spectra with the inverse of the down-conversion factor $f_{\mathrm{rep}}/\Delta f_{\mathrm{rep}}$ results in spectra that lie in the of-domain, nonetheless, the known position of the Rb absorption line in the of-regime at 377.211 THz is necessary to calculate the frequency shift in order to bring the spectra to an absolute-frequency scale. The resulting spectrum is depicted in the bottom part of figure 3.14.
Averaging over all spectra yields the average spectrum depicted in figure 3.13. The retrieved spectrum looks similar to the spectrum generated by averaging over the bursts of the IFG, however, the absorption line of Rb is much more distinct with a width of 0.3 nm (103 GHz). Comparison of this resolution to the natural linewidth of $\Gamma = 2\pi{\cdot}5.7500(56)$ MHz and the Doppler-broadened linewidth of $\Gamma_{\mathrm{Doppler}} = 402.2$ MHz shows, that the setup did not yet achieve its desired resolution.

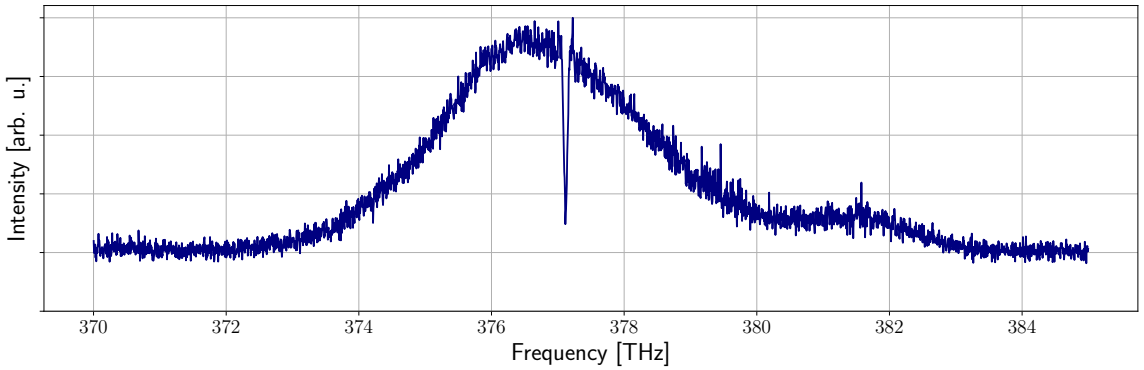

Figure 3.13.: **Average over all spectra retrieved from the interferometric bursts.** The Rb absorption is clearly visible.

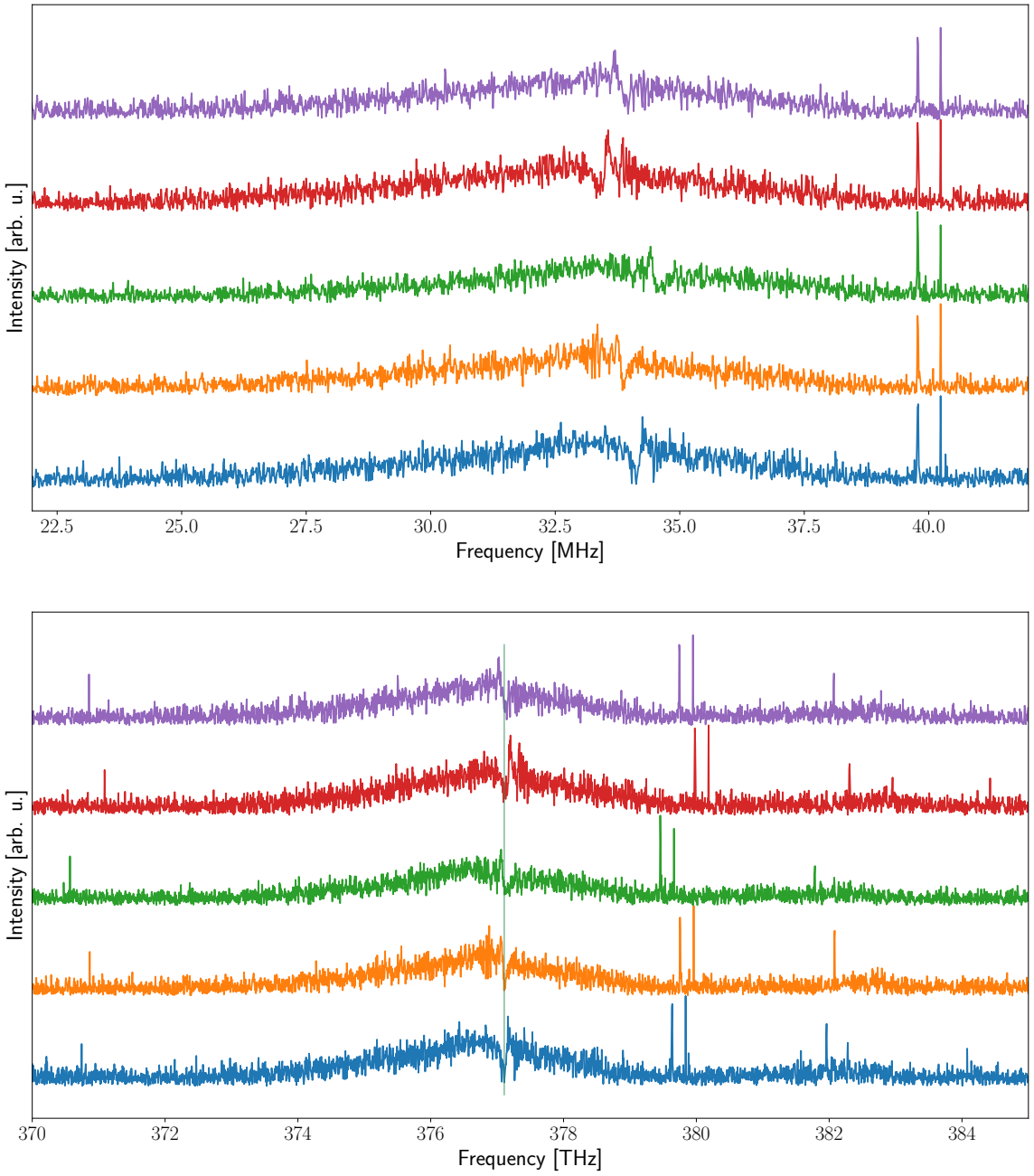

Figure 3.14.: **Selected spectra calculated by Fourier-transformation of the single bursts in the IFG. Top:** rf-domain spectra before up-conversion. **Bottom:** of-domain spectra after up-conversion and offset. The position of the Rb line is shown as a green vertical line.

4. Numerical Model

4.1. Kalman-Filter

In order to predict the interferometric data expected in the experiment, particularly the influence of fluctuations in the repetition rate f_{rep} and the carrier envelope offset f_0 ($\equiv f_{\mathrm{CEO}}$) on the IFG, a numerical simulation was performed. The effect of fluctuations is depicted in figure 4.1. While fluctuations of the carrier envelope phase shift the spectrum equally, since all modes are effected evenly, fluctuations in the repetition rate cause a "breathing" of the spectrum.

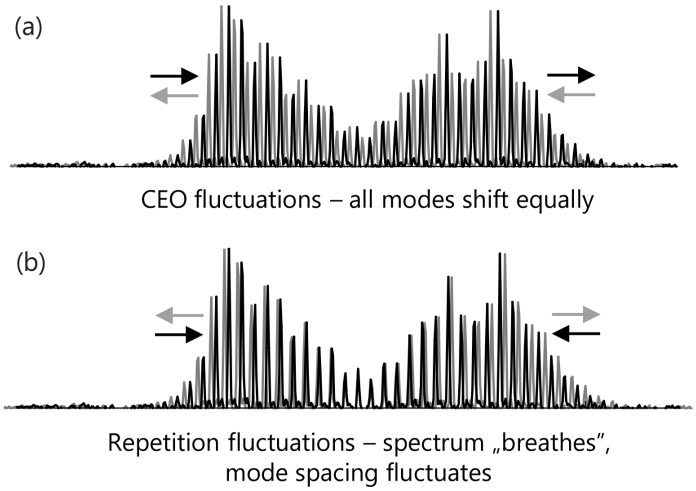

Figure 4.1.: **Influences of fluctuations on the rf spectrum.**
Top: f_0 fluctuations **Bottom:** f_{rep} fluctuations.
Image taken from [28]

To determine the severity of fluctuations on the interferometric data a *MATLAB* code, developed by Burghoff et al. [5] was translated to *Python* to provide a better understanding and compatibility. Originally, the code was used to demonstrate a computational phase correction of DCS data in [5] and adapted with the intention to correct experimental data recorded in the course of this thesis. The correction algorithm uses an augmented Kalman filter. However, the full treatment of this algorithm is beyond the scope of this work and can be found in [5].

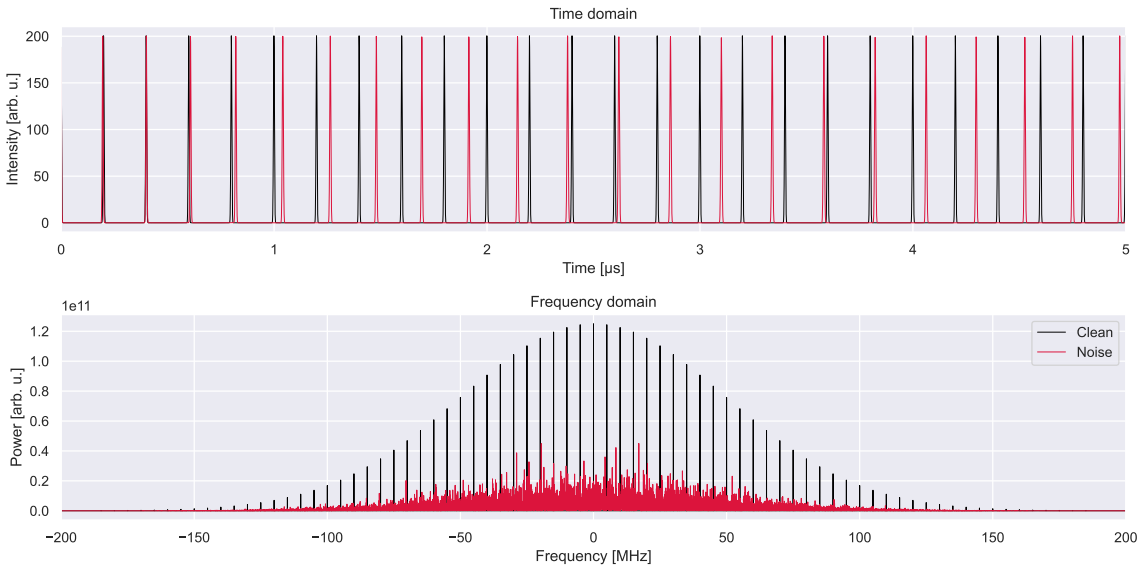

Figure 4.2.: **Artificially generated DCS data. Top:** Pulses in the time-domain with a mean repetition rate of $f_{\mathrm{rep}} = 5\,\mathrm{MHz}$, with (red) and without (black) fluctuations of the repetition rates, as well as carrier envelope frequency. **Bottom:** rf-spectrum retrieved via FT Fourier-transformation, of the clean and noisy data, in black and red, respectively. The amplitude of the former was increased by a factor of 10 to allow better display.

Simulating the expected data retrieved from the interferograms gives insight into the influence of fluctuations of f_0 and f_{rep}, as illustrated in the bottom part of figure 4.2. It is clearly visible that fluctuations do not only affect the discrete separation of the lines in the retrieved rf spectrum and lead to a continuous spectrum without distinguishable comb lines. They also significantly reduce the power of the spectral lines, since their power is distributed to a continuum. This highlights the importance of a proper stabilization of both parameters to enhance the resolution of the setup. While the use of a Kalman filter in principle allows for a reconstruction of the rf modes, it has been proven to be computationally challenging and its real-time application is limited to DCS systems with few modes [28]. Since the OFCs used in this experiment cover a large spectral width with a high repetition rate, the number of modes $M = \Delta\nu / f_{\mathrm{rep}} \approx 120\,000$ exceeds the limit of practical use by far, therefore it was not further investigated here. The original code can be found at [14].

4.2. Simulation of expected interferograms

To demonstrate the expected modulation of the interferograms due to absorption transitions, the influence of absorption was simulated. The electric field of the pulse can be considered as the superposition of plane monochromatic waves:

$$E_k(t) = \sum_n A_{n,k} \exp[-2\pi i \nu_{n,k} t] + c.c., \tag{4.1}$$

with *c.c.* denoting the complex conjugate and $A_{n,k}$ the amplitude of the n-th mode of the k-th OFC. With the complex refractive index $\underline{n} = n - i\kappa$, the electric field behind the sample (of the OFC that passes the sample) can be written as:

$$E_k(t) = \sum_n A_{n,k} \exp[-2\pi i \nu_{n,k} t] \exp[-2\pi \kappa x \nu_n / c] + c.c., \tag{4.2}$$

with c denoting the speed of light inside the medium and x the distance the light beam travelled within the sample. Since the total electric field is determined by both OFCs, the total electric field is the sum of the two fields $E(t) = E_1(t) + E_2(t)$, consequently the intensity on the photo detector is proportional to

$$I(t) \propto [E_1(t) + E_2(t)][E_1(t) + E_2(t)]^*. \tag{4.3}$$

Considering only the beating between neighbouring comb modes the intensity can be written as

$$I(t) \propto \sum_n 2A_{n,1}A_{n,2} \exp[-4\pi \kappa x \nu_n / c] \cos[2\pi(\nu_{n,1} - \nu_{n,2})t] \tag{4.4}$$

Using the equation above allows to simulate the interferogram and calculate the rf-spectrum, as well as the of-spectrum including the effects of absorption. For the simulation the Rubidium D_1 transition ($5^2P_{1/2} \rightarrow 5^2S_{1/2}$) at 794.760 nm, as well as the hyperfine splitting ($F = 1, 2$) is considered. A detailed overview of the level scheme is given in figure 2.7. For the extinction coefficient a value of $\kappa = 2.0314$ [26] was used and the FWHM of the natural linewidth is assumed to be $\Gamma = 2\pi \cdot 5.7500(56)$ MHz [27].

In order to be able to compare the experimentally measured spectra to the simulation the same parameters as in the experiment were chosen for the simulation. More specifically, the spectra were chosen to have a width of $\Delta\nu = 21.8$ nm, spanning from 782.8 nm to 804.6 nm with a Gaussian line-shape. The optimum repetition rate difference was calculated to 308 Hz and a sampling frequency of $f_s = 80.0003$ MHz was set.

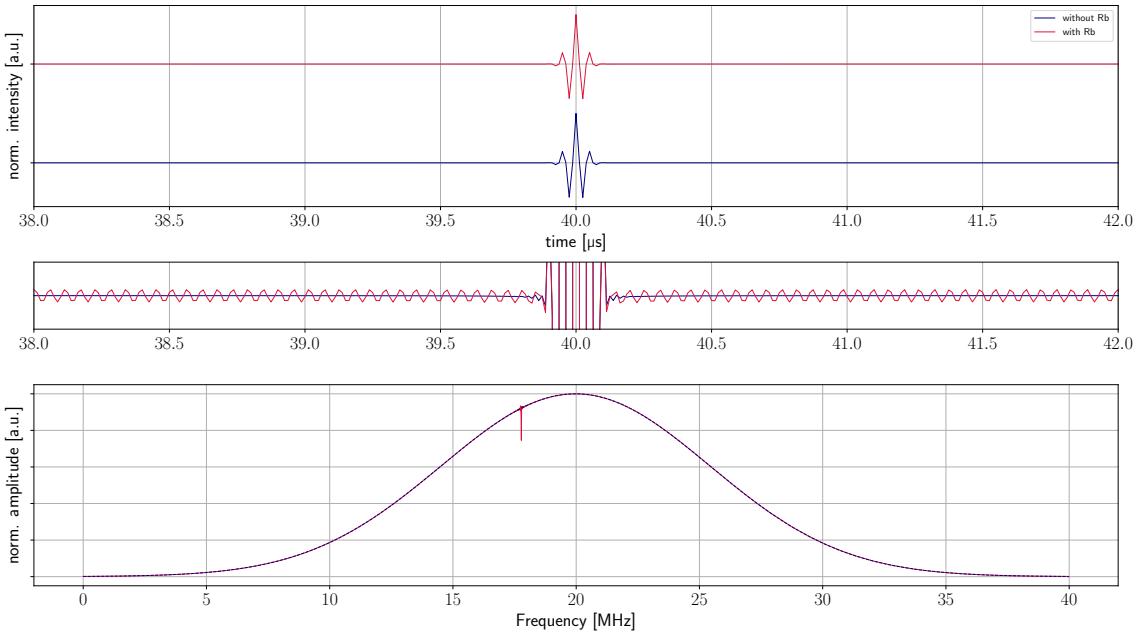

Figure 4.3.: **Simulated IFG and its Fourier transform. Top:** Cutout of the simulated IFG with (red) and without (blue) the Rb sample considered. **Middle:** Zoom in on the IFGs shown in the top to highlight the polarization decay. **Bottom:** Fourier-transformation of the simulated IFG. The D_1 absorption line is clearly visible.

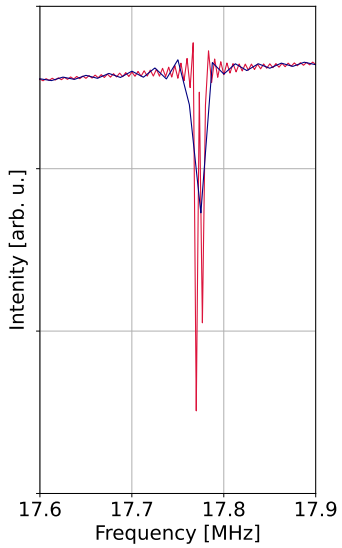

Figure 4.4.: Comparison of the resolution of the 80 μs (blue) and 300 μs (red) long IFG.

Simulating with these parameters yields the IFGs shown in the top part of figure 4.3, with and without the Rb sample, respectively. The "wiggeling" tail of the IFG including the Rb sample is visible when zooming in, shown in the middle part of figure 4.3. Performing the Fourier transform of a 80 μs long time trace centred around the peak of the IFG yields the rf-spectra shown in the bottom part of figure 4.3 including (red) and without (blue) the Rb sample. Since the rf and the of-spectra are equal except for dilation and offset, no up-conversion was performed. The absorption of the Rb D_1 transition is clearly visible and has a resolution of $\Delta f \approx 37.56\,\text{kHz}$ in the rf-domain, corresponding to $\Delta\nu \approx 9.756\,\text{GHz}$ (0.021 nm) in the of-domain. While the absorption line is clearly visible, the hyperfine splitting could not be observed, since the resolution is limited by the acquisition time of the IFG. Increasing the length of the analysed time trace to 300 μs allows resolving the

$F = 1$ and $F = 2$ level. Figure 4.4 depicts the difference between the short (red) and long (blue) analysis of the IFG, clearly showing the improved resolution by increasing the length of the time trace. Due to fluctuations in the repetition rate, this is not feasible in the experiment, since it leads to "washing out" of the spectral line.

In order to investigate the influence of fluctuations in the repetition rate on the spectra, the simulation was repeated with the same parameters as above, except for a broader absorption line[1], assumed to have a width of $2\pi \cdot 30\,\mathrm{MHz}$. Random fluctuations in the range of $\pm 0.8\,\mathrm{Hz}$ (which equals a change in cavity length of $\pm 20\,\mathrm{nm}$) was assumed for both OFCs, the Fourier transform of the interferograms is shown in figure 4.5. The effect of fluctuations is clearly visible, significantly reducing the resolution and absorbance of the absorption line compared with the spectrum containing no fluctuations (figure 4.5, right).

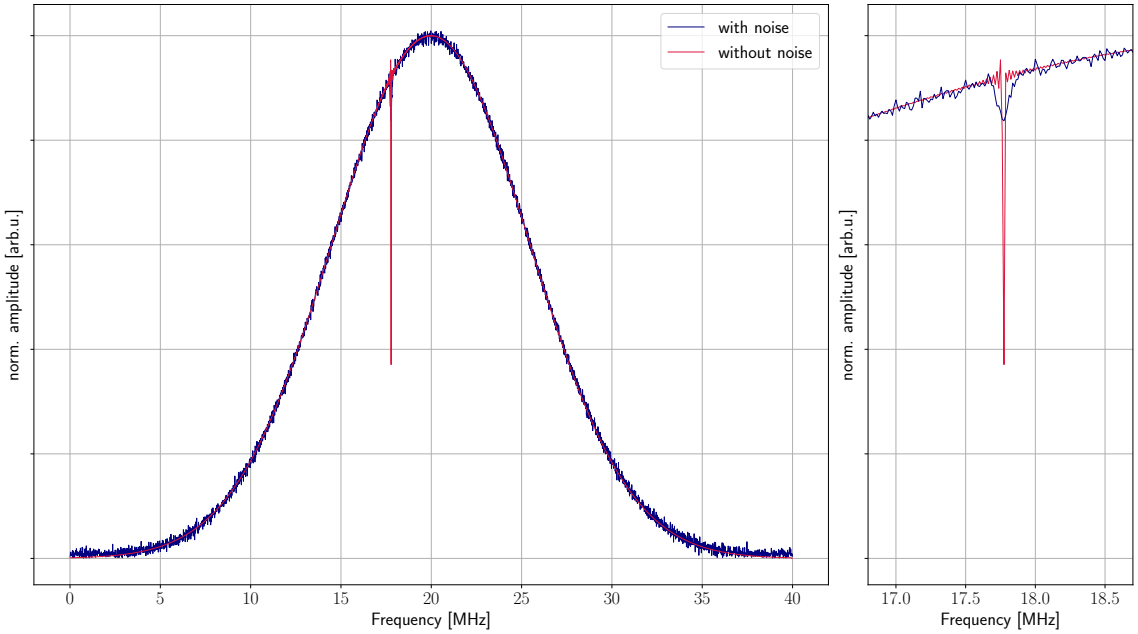

Figure 4.5.: **Spectra of simulated IFG containing fluctuations. Left:** Fourier transform of the simulated IFG with (blue) and without (red) fluctuations. **Right:** Cut-out of the spectra around the absorption line.

[1]This significantly enhanced the visibility of the effects of fluctuations on the spectra.

5. Summary and Outlook

The primary aim of this thesis was the setup and implementation of two frequency combs to perform dual-comb spectroscopy. Since the laser systems were used elsewhere prior to this experiment, several conversions were necessary. This included converting one of the frequency combs from picosecond to femtosecond operation, as well as replacing multiple mirrors to compensate for the malfunction of one of the pump lasers.
Subsequently, the electronics required for stable mode-locked operation and the cavity-length control, as well as the chiller for temperature stabilization were set up. After coupling the pump laser beams into the respective frequency combs, they were adjusted and cw lasing was achieved for both frequency combs.

Afterwards, the systems were mode-locked, which required optimizing the signal of the photodiode measuring the repetition rate by adjusting its position, as well as setting a proper phase on the mode-locking electronics module. After stable mode-locked operation was achieved for both frequency combs, it was found that while the coarse cavity-length adjustment worked for both systems, the fine rapid stabilization with the piezo-electric motor did not work properly for the first frequency comb. Additionally, the repetition rate displayed on the *Model 3930* control units was found to deviate from the repetition rate measured with a photo-detector. However, since the interferometric signal only depends on the repetition rate difference between the two combs and the display is limited to the hundreds place the displayed value still serves as a coarse guidance.

Once mode-locking was achieved, the frequency combs' spectra and output powers were optimized by changes in the prism compressor and the orientations of the cavity end mirrors, respectively. This could be done without opening the frequency combs' protective cover by adjustment screws and micrometer heads accessible at the top.

In order to improve and facilitate the data acquisition and analysis, the oscilloscope used in the beginning was replaced, to allow for data acquisition with the help of a python script. This also allowed longer time-traces to be recorded to improve the resolution. The data acquisition could be further improved through a dedicated fast ADC system with finer resolution (16-bit in lieu of 10-bit). Additionally, a low-pass was connected to the photo detector output to suppress beating frequencies above 40 MHz for an unambiguous assignment of the beat modes.

Subsequently, the beam path for the generation of the heterodyne beating was set up and the first interferograms were recorded and analysed. The spectra were calculated by averaging the interferometric bursts of the time-trace after phase correction and performing the Fourier transform. With this data-analysis routine it was possible to retrieve the spectra of the Rb sample with a resolution of up to 30 GHz. However, limited averaging was possible, due to fluctuations of the repetition rates caused by the lack of stabilization due to the malfunctioning electronic control unit

of one of the lasers. Additionally, a double periodic structure in the interferograms was visible, caused by double pulses from the frequency combs. However, this does not pose a problem as long as the modulation is not overlapped by the second burst which would effectively double the number of bursts inside a time interval.

To diminish the influence of repetition rate fluctuations of the frequency combs, an adaptive sampling routine was added to the data analysis which greatly improved the possibility to average and thereby the resolution of the measurement. A second data set was recorded for which the resolution could be improved using the adaptive sampling analysis. However, with a resolution of 240 GHz it remained below the resolution achieved for the previous data set, since only two third of the maximum in repetition rate difference were used. This shows the importance of utilizing the total spectral range in the radio frequency regime to improve the resolution.

Averaging over the spectra from single bursts rather than averaging over the bursts before Fourier-transformation improved the resolution to 103 GHz for the second data set. Since this analysis routine requires a known spectral reference in order to bring the spectra to an absolute frequency scale, it could prove to be advantageous to utilize a reference cell with known spectral features, in order to average spectra of interest. This would enhance the recording length, since only one channel needs to be recorded or could potentially be combined with the adaptive sampling routine.

To correct for fluctuations in the repetition rate, the use of a Kalman filter was considered, however its application is limited to dual-comb systems containing only a few modes and is therefore not feasible for the experiment presented in this thesis. Despite this, the influence of repetition rate fluctuations on a resolved comb structure could be investigated.

In order to determine the possible resolution and analyse the influence of repetition rate fluctuations, multiple simulations of the interferograms and their respective spectra were performed, clearly showing the importance of long averaging times which considerably enhanced the resolution of the simulated spectra. Additionally, introducing a random fluctuation of ± 0.8 Hz to the repetition rate (which corresponds to a cavity length difference of ± 20 nm) for both frequency combs, clearly showed the decrease in resolution in the spectra.

Stabilizing the repetition rate with the piezo-electric motor would improve the averaging capability and subsequently increase the resolution. This could potentially enable to Fourier transform the entire interferogram, thereby drastically improving the resolution and enabling broadband high resolution spectroscopy. Phase locking the frequency combs could potentially increase the resolution to the order of MHz. Additionally, using an external reference could further improve the resolution to the order of kHz and enable long-term averaging, as well as an absolute frequency scale without the use of a reference cell.

6. Acknowledgements

First of all I would like to thank **Thomas Pfeifer** for giving me the opportunity to be a part of his division and supervising this Bachelor-thesis. Your passion and excitement has really been inspiring.

I would like to thank **José Crespo** for taking on the role as second supervisor of this thesis.

Moreover I would like to thank **Christian Ott** for giving me the opportunity to write this thesis in his group.

I am particularly thankful to **Max Hartmann** for overseeing this thesis and our many great hours in the lab. It has been a lot of fun working with and learning from you. Without you I would have never come across this interesting topic.

Special thanks to **Felix Klein** for our many helpful discussions - not just about DCS and your great help in the setup of this experiment.

Furthermore I would like to thank all the awesome people at the MPIK for such a wonderful time. Special thanks to **Marc Rebholz** for proofreading this thesis.

Not least I am deeply grateful for all the love and support from my family and friends - without you none of this would have been possible.

A. Pump Laser Details

The two pump laser used in the scope of this thesis use the transitions of Nd^{3+} ions doped in doped in a yttrium vanadate crystalline matrix (Nd:YVO_4). The energy levels of Nd^{3+} are shown in figure A.1.

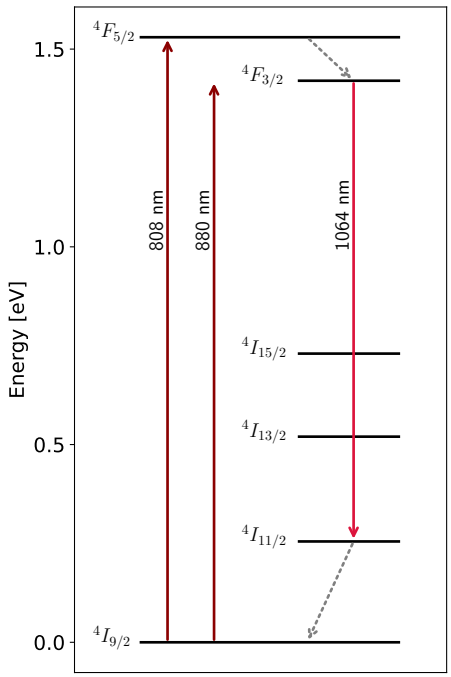

Figure A.1.: **Energy level scheme for Nd^{3+}**

Laser transmission is achieved by a four level energy scheme, where the a 808 nm semiconductor laser excites the atom from its ground level to the excited level $^4I_{9/2} \rightarrow {}^4F_{5/2}$ and quickly decays by non radiative transmission to the $^4F_{3/2}$ level (in fig. A.1 shown as the grey arrow). From this level it decays radiatively from to the $^4I_{11/2}$ level with emission at 1064 nm and subsequent, again by non radiative transmission to back to the $^4I_{9/2}$, creating a population inversion between the $^4F_{3/2}$ and the $^4I_{11/2}$ level, thus amplifying through-passing light as an active medium. The 1064 nm emission is then frequency doubled by a lithium-triborate crystal (LBO), resulting in the 532 nm light used for pumping the Ti:Sa crystal.

For simplification the Stark levels are not shown in figure A.1. Laser emission also occurs from the $^4F_{3/2} \rightarrow {}^4I_{13/2}$ and $^4F_{3/2} \rightarrow {}^4I_{9/2}$ at 1340 nm and 914 nm, respectively, whilst being less probable than the principal $^4F_{3/2} \rightarrow {}^4I_{11/2}$ transition. [16, 22]

B. Figures

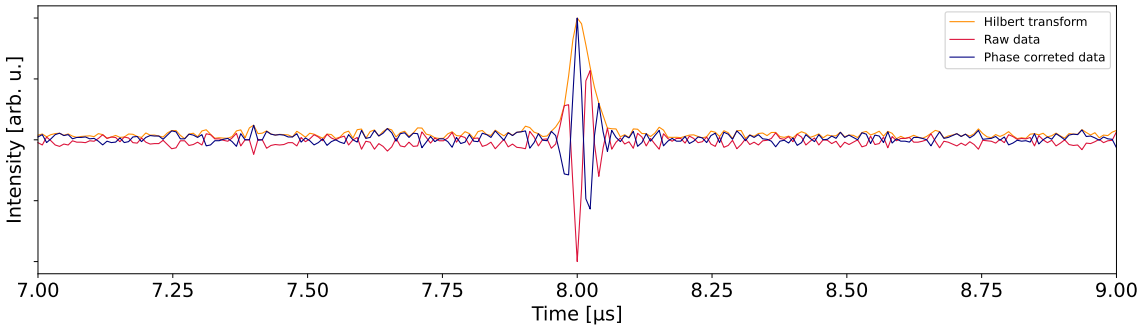

Figure B.1.: **Example phase correction of the IFG bursts.** Calculating the Hilbert transform (orange) of the raw data (red) allows to correct the phase of the bursts, such that their phase is zero (blue).

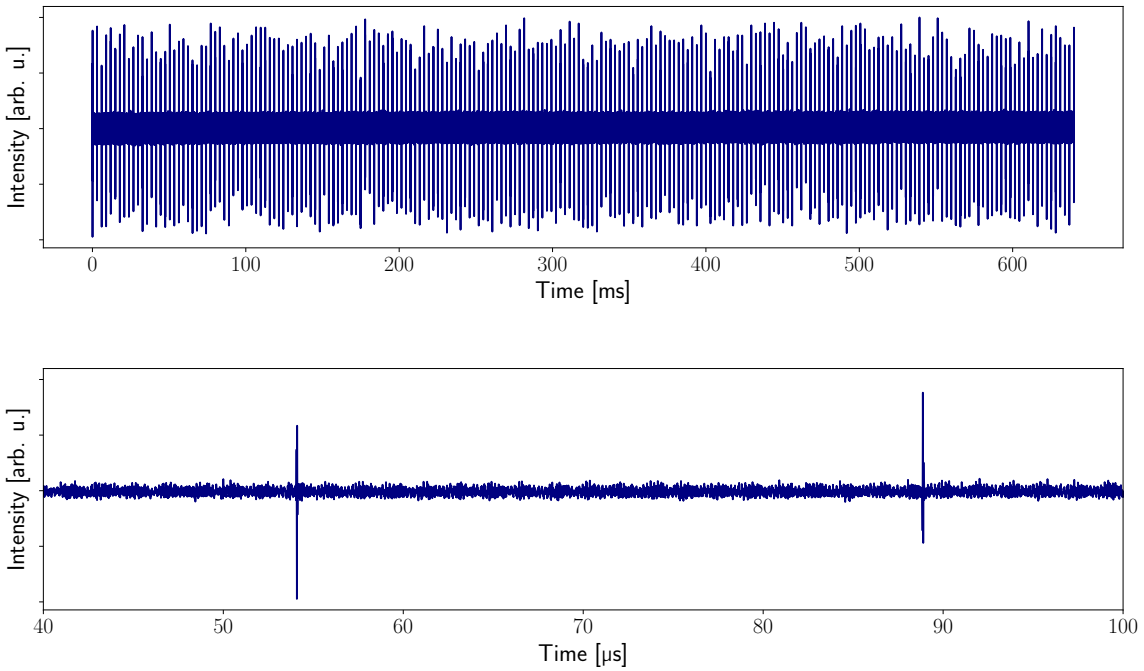

Figure B.2.: **Time-trace of the first measurement with the Rb sample.**
Top: complete interferogram containing 217 double-bursts.
Bottom: Zoom in on double-bursts separated by 34.8 μs.

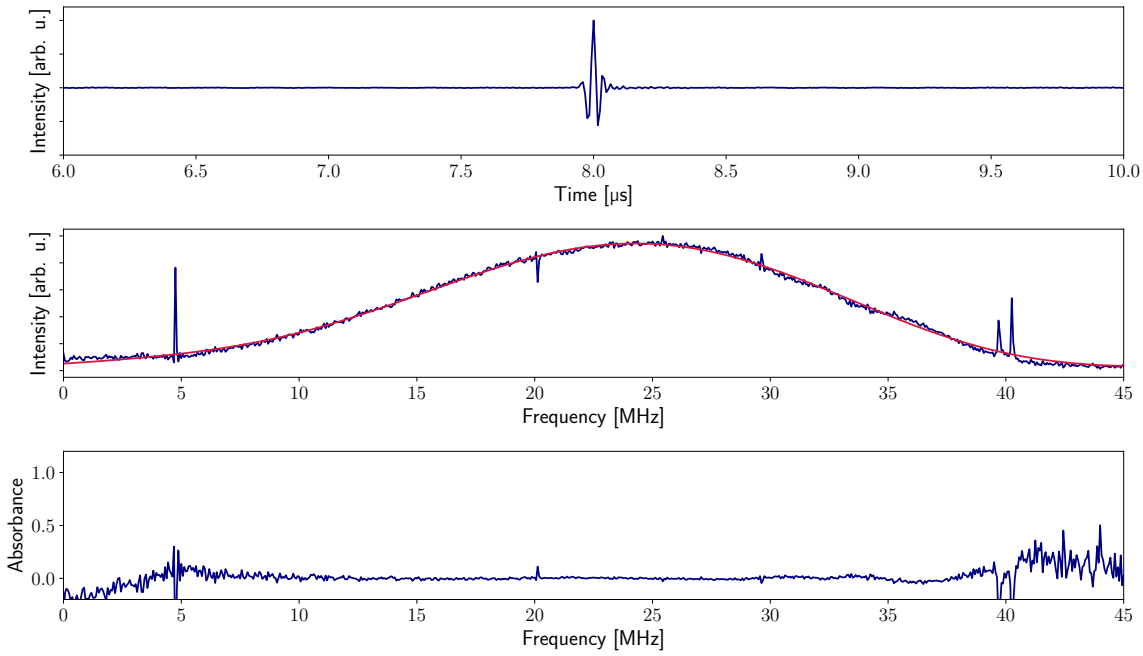

Figure B.3.: **Average over the full time-trace of the first measurement with the Rb sample. Top:** Averaged IFG burst. **Middle:** Spectrum calculated by Fourier-transformation of the averaged burst (blue) and low-passed spectrum (red) **Bottom:** Absorbance calculated by comparison of the spectrum and the low-passed spectrum.

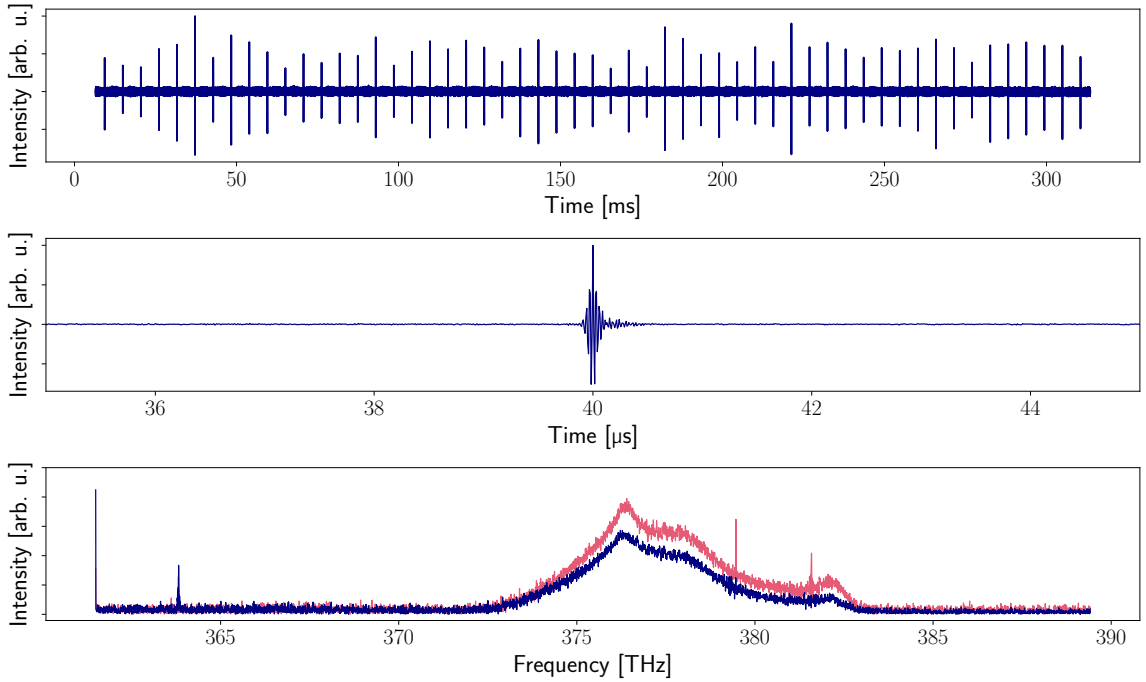

Figure B.4.: **Measurement without Rb cell present. Top:** Recorded time-domain IFG. **Middle:** Averaged IFG bursts. **Bottom:** Spectrum generated by Fourier-transformation of the averaged IFG bursts with (blue) and without (red) adaptive sampling.

Bibliography

[1] „A Scanning Grating Spectrograph With A Lead-Sulphide Detector. I. The Experimental Equipment“. In: *Arkiv Fysik* Vol: 20 (Jan. 1961).

[2] R. Adair, L. L. Chase, and S. A. Payne. „Nonlinear refractive index of optical crystals“. In: *Phys. Rev. B* 39 (5 Feb. 1989), pp. 3337–3350. DOI: 10.1103/PhysRevB.39.3337.

[3] S. Akturk et al. „Extremely simple single-prism ultrashort-pulse compressor“. In: *Opt. Express* 14.21 (Aug. 2006), pp. 10101–10108. DOI: 10.1364/OE.14.010101.

[4] B. Bernhardt. „Dual Comb Spectroscopy“. 2011.

[5] D. Burghoff, N. Han, and J. H. Shin. „Generalized method for the computational phase correction of arbitrary dual comb signals“. In: *Opt. Lett.* 44.12 (June 2019), pp. 2966–2969. DOI: 10.1364/OL.44.002966.

[6] I. Coddington, N. Newbury, and W. Swann. „Dual-comb spectroscopy“. In: *Optica* 3.4 (Apr. 2016), pp. 414–426. DOI: 10.1364/OPTICA.3.000414.

[7] I. Coddington, W. C. Swann, and N. R. Newbury. „Time-domain spectroscopy of molecular free-induction decay in the infrared“. In.

[8] J.-C. Diels and W. Rudolph. *Ultrashort Laser Pulse Phenomena, 2nd Edition.* eng. 2nd edition. Online resource; Title from title page (viewed September 21, 2006). Academic Press, 2006.

[9] T. Fortier and E. Baumann. „20 years of developments in optical frequency comb technology and applications“. In: *Communications Physics* (2019). DOI: 10.1038/s42005-019-0249-y.

[10] J. Fraunhofer. „Bestimmung des Brechungs- und des Farbenzerstreungs-Vermögens verschiedener Glasarten, in Bezug auf die Vervollkommnung achromatischer Fernröhre“. In: *Annalen der Physik* 56.7 (1817), pp. 264–313. DOI: https://doi.org/10.1002/andp.18170560706.

[11] S. Galtier, C. Pivard, and P. Rairoux. „Towards DCS in the UV Spectral Range for Remote Sensing of Atmospheric Trace Gases“. In: *Remote Sensing* 12.20 (2020). DOI: 10.3390/rs12203444.

[12] S. M. Holzner. „Dual-Comb Spectroscopy of Fundamental Vibrational Transitions“. 2015.

[13] T. Ideguchi et al. „Adaptive real-time dual-comb spectroscopy“. In: *Nature Communications 2014 5:1* 5 (1 Feb. 2014). Ref. 7, pp. 1–8. DOI: 10.1038/ncomms4375.

[14] *Kalman filter Code by Burghoff et al.* https://github.com/burghoff/turbo-comb. Accessed: 2022-05-01.

[15] C. Khurmi et al. „Self-corrected chip-based dual-comb spectrometer“. In: *Optics Express, Vol. 25, Issue 7, pp. 8168-8179* 25 (7 Apr. 2017), pp. 8168–8179. DOI: 10.1364/OE.25.008168.

[16] C. C. Kores, J. J. Neto, and N. U. Wetter. „Comparison of grazing incidence Nd:YVO4 lasers pumped at 808 and 880 nm“. In: *Advanced Solid-State Lasers Congress* (2013), ATu3A.10. DOI: 10.1364/ASSL.2013.ATu3A.10.

[17] R. Liao et al. „Dual-comb generation from a single laser source: principles and spectroscopic applications towards mid-IR—A review“. In: *Journal of Physics: Photonics* 2 (4 Sept. 2020), p. 042006. DOI: 10.1088/2515-7647/ABA66E.

[18] Z. Liu et al. „Phase Reconstruction of Strong-Field Excited Systems by Transient-Absorption Spectroscopy“. In: *Phys. Rev. Lett.* 115 (3 July 2015), pp. 033003-1–033003-5. DOI: 10.1103/PhysRevLett.115.033003.

[19] O. E. Martinez, J. P. Gordon, and R. L. Fork. „Negative group-velocity dispersion using refraction“. In: *J. Opt. Soc. Am. A* 1.10 (Aug. 1984), pp. 1003–1006. DOI: 10.1364/JOSAA.1.001003.

[20] I. Newton. *Opticks*. Dover Press, 1704.

[21] N. Picqué and T. W. Hänsch. „Frequency comb spectroscopy“. In: *Nature Photonics* (Mar. 2019), pp. 146–157. DOI: https://doi.org/10.1038/s41566-018-0347-5.

[22] B. E. A. Saleh and M. C. Teich. *Fundamentals of photonics*. eng. 2. ed. Wiley series in pure and applied optics. Hoboken, N.J.: Wiley, 2007, XIX, 1177 S.

[23] Y. Sato et al. „Laser operation with near quantum-defect slope efficiency in Nd:YVO4 under direct pumping into the emitting level“. In: *Applied Physics Letters* 82.6 (2003), pp. 844–846. DOI: 10.1063/1.1544659.

[24] S. Schiller. „Spectrometry with frequency combs“. In: *Opt. Lett.* 27.9 (Mar. 2002), pp. 766–768. DOI: 10.1364/OL.27.000766.

[25] S. Schilt and T. Südmeyer. „Carrier-Envelope Offset Stabilized Ultrafast Diode-Pumped Solid-State Lasers“. In: *Applied Sciences* 5.4 (2015), pp. 787–816. DOI: 10.3390/app5040787.

[26] N. V. Smith. „Optical Constants of Rubidium and Cesium from 0.5 to 4.0 eV“. In: *Phys. Rev. B* 2 (8 Oct. 1970), pp. 2840–2848. DOI: 10.1103/PhysRevB.2.2840.

[27] D. A. Steck. *Rubidium 87 D Line Data*. URL: https://www.steck.us/alkalidata/rubidium87numbers.pdf.

[28] L. A. Sterczewski, J. Westberg, and G. Wysocki. *Computational coherent averaging for free-running dual-comb spectroscopy*. 2019. DOI: 10.1364/OE.27.023875.

[29] W. H. Wollaston. „XII. A method of examining refractive and dispersive powers, by prismatic reflection“. In: *Philosophical Transactions of the Royal Society of London* 92 (1802), pp. 365–380. DOI: 10.1098/rstl.1802.0014.

[30] T. Yasui et al. „Adaptive sampling dual terahertz comb spectroscopy using dual free-running femtosecond lasers“. In: *Nature Publishing Group* (2015). DOI: 10.1038/srep10786.

C. Erklärung

Ich versichere, dass ich diese Arbeit selbstständig verfasst und keine anderen als die angegebenen Quellen und Hilfsmittel benutzt habe.

Heidelberg, den 28.07.2022 

(Finn Lubenau)